

In presenting this dissertation in partial fulfillment of the requirements for an advanced degree at Idaho State University, I agree that the Library shall make it freely available for inspection. I further state that permission for extensive copying of my dissertation for scholarly purposes may be granted by the Dean of the Graduate School, Dean of my academic division, or by the University Librarian. It is understood that any copying or publication of this dissertation for financial gain shall not be allowed without my written permission.

Signature \_\_\_\_\_

Date \_\_\_\_\_

POSITRON PRODUCTION EFFICIENCY STUDY USING  
HIGH REPETITION RATE LINAC AT IAC

by

Sadiq Setiniyaz  
(Shadike Saitiniyazi)

A dissertation

submitted in partial fulfillment

of the requirements for the degree of

Doctor of Philosophy in the Department of Physics

Idaho State University

Jul 2013

©Copyright

by

Sadiq Setiniyaz

(Shadike Saitiniyazi)

2013

To the Graduate Faculty:

The members of the committee appointed to examine the dissertation of Sadiq Setiniyaz (Shadike Saitiniyazi) find it satisfactory and recommend that it be accepted.

---

Tony Forest, Ph.D.

Major Advisor

---

Yujong Kim, Ph.D.

Committee Member

---

Dustin McNulty, Ph.D.

Committee Member

---

Mahbub A. Khandaker, Ph.D.

Committee Member

---

Wenxiang Zhu, Ph.D.

Committee Member

# Contents

	Page
Acknowledgements . . . . .	i
Table of Contents . . . . .	ii
List of Figures . . . . .	iv
List of Tables . . . . .	viii
Abstract . . . . .	ix
<b>Chapter</b>	
1 Introduction . . . . .	1
1.1 Positron Beam . . . . .	1
1.1.1 Positron Beam for Positron Annihilation Spectroscopy . . . . .	1
1.1.2 Positron Beam for Measuring The Impact of Two Photon Exchange . . . . .	2
1.2 Positron Beam Generation from Bremsstrahlung . . . . .	3
1.3 Emittance Measurement . . . . .	7
1.3.1 Emittance . . . . .	8
1.3.2 Emittance Measurement . . . . .	9
1.3.3 Quadrupole Scanning Method . . . . .	10
2 Apparatus . . . . .	14
2.1 HRRL Beamline . . . . .	14
2.2 The OTR Imaging System . . . . .	16
2.3 Positron Detection . . . . .	18
2.3.1 NaI Detectors . . . . .	19
2.3.2 The DAQ Setup . . . . .	23
3 Simulation . . . . .	27
3.1 Step 1 - The Electron Beam Generation and Transportation to T1 . . . . .	27
3.1.1 The Positron Beam on DDNT1 . . . . .	28

3.1.2	The Positron Beam on Virtual Detectors DQ4 and DD1 . . . . .	31
3.2	Step 2 - The Transportation of The Positron Beam from DDNT1 to The Entrance of The First Dipole . . . . .	32
3.3	Step 3 - The Transportation of Positrons from the Entrance of The First Dipole to T2 and The Detection of 511 keV Photons . . . . .	34
3.3.1	Positrons Detected by The Detection System . . . . .	35
3.3.2	Beam Loss Study . . . . .	35
3.3.3	Analysis of the Photon Count Asymmetry in NaI Detectors . . . . .	41
3.4	Quadrupole Triplet Collection Efficiency Study . . . . .	44
3.5	Systematic Errors . . . . .	45
4	Data Analysis . . . . .	48
4.1	HRRL Emittance Measurement . . . . .	48
4.2	Measurement of HRRL Electron Beam Energy Spread at 12 MeV . . . . .	52
4.3	The Electron Beam Current Measurement . . . . .	53
4.4	Positron Rate Estimation in Coincidence Mode . . . . .	56
4.5	The Positron Production Runs . . . . .	56
4.6	Positron Rate Estimation in OR Mode . . . . .	59
4.7	Positron to Electron Ratio . . . . .	59
5	Conclusions and Suggestions . . . . .	62
A	The Electron Beam Energy Scan . . . . .	65
B	MATLAB Scripts for Calculating Emittance . . . . .	68
B.1	Emittance Calculator . . . . .	68
B.2	Super Gaussian Fit . . . . .	80
B.3	Parabolic Fit . . . . .	80
	References . . . . .	86

# List of Figures

1.1	Form factor ratio (R), obtained using the Rosenbluth Technique (hollow squares) [3] and from the Recoil Polarization Technique (solid circles) [5]. . . . .	2
1.2	Photon emission from the bremsstrahlung processes. . . . .	3
1.3	Bremsstrahlung photon energy distribution produced when the 12 MeV electron energy distribution from Figure 1.4 interacts with the simulation's 1 mm thick tungsten target. . . . .	4
1.4	The electron energy distribution incident on a tungsten foil in simulation. . .	5
1.5	The cross-sections for different types of photon interactions with tungsten as a function of photon energy [10]. . . . .	6
1.6	Pair production. . . . .	7
1.7	Photon spectrum of created by million 12 MeV mono energy electrons impinging on a 1.016 mm thick tungsten target. . . . .	8
1.8	Coordinated system and reference orbit (dashed line) [11]. . . . .	9
1.9	Apparatus used to measure the beam emittance. . . . .	11
2.1	The configuration of the HRRL cavity. . . . .	15
2.2	The HRRL beamline layout and parts. . . . .	17
2.3	The OTR imaging system. . . . .	18
2.4	The positron detection system: T2 (pink) was placed with 45° angle to the horizontal plane first, then rotated 45° along the vertical axis. . . . .	19
2.5	The NaI crystal dimension. . . . .	20
2.6	The modified PMT base design. . . . .	21
2.7	The NaI crystals and new bases. . . . .	22

2.8	Detector output pulses using the Co-60 source and new PMT. The amplitude of the pulse is about 60 mV. The rise time of the pulse is larger than 50 ns, and the fall time is larger than 700 ns. . . . .	22
2.9	The calibrated NaI spectrum of Na-22 and Co-60 sources. . . . .	23
2.10	The 511 keV peak observed using NaI detectors shifted when accelerator RF was on. The spectrum were taken with RF on (dotted line) and with RF off (dashed line). The solid line represents the photon spectrum created by 3 MeV positrons impinging on T2. . . . .	24
2.11	The DAQ setup and timing diagram. . . . .	26
3.1	T1 is the positron production target. DUPT1 is a virtual detector located upstream of T1 to detect the incoming electron beam. DDNT1 is a virtual detector downstream of T1. DT1 is a virtual detector that is placed right after T1 parallel to it. . . . .	28
3.2	Energy distribution of incident electrons (dotted dashed line), electrons after T1 (dashed line) and created positrons (solid line). The incident electron distribution counts were weighted by 0.001. . . . .	29
3.3	The transverse beam projections and angular distributions of positrons detected. . . . .	30
3.4	The geometry of the target T1 and the virtual detector DDNT1. . . . .	31
3.5	The positron beam $y'$ vs. $y$ detected by DDNT1. . . . .	32
3.6	The positron beam energy distribution detected downstream of T1. . . . .	33
3.7	The generation and transportation of the positron beam in step 2. The virtual detectors were used to track the positrons. . . . .	34
3.8	T2 and virtual detectors located upstream (DT2UP) and downstream (DT2DN) of T2 are shown at the center of the figure. NaI detectors and Pb shielding are located horizontally at two sides. . . . .	34



3.9	NaI detector efficiency obtained from Saint-Gobain Crystals [20]. The lines correspond to the different crystal sizes (in inches) shown on the right side of the figure. . . . .	36
3.10	Positrons detected on virtual detector DDNT1 and 511 keV photon pairs detected by the NaI detectors in coincidence mode when Q7 is at 0 A, 3.5 A and 10 A. . . . .	37
3.11	Predicted number of positrons transported. Black cube: positrons incident on DDNT1. Red cube: positrons entered Q4. Blue cube: positrons entered D1. Magenta cube: positrons exited D1. Black circle: positrons entered Q7. Red circle: positrons entered D2. Blue circle: positrons exited D2. Magenta circle: positrons incident on DT2UP. Black triangle: 511 keV photons detected by NaI detectors in coincidence mode. . . . .	39
3.12	Positrons transported when dipoles are set to bend 3 MeV positrons. . . . .	41
3.13	NaI detector locations around T2. The positron beam (blue line) is traveling along the z-axis (into the paper). (a) T2 was rotated clockwise about the x-axis by 45° positioning the upstream side of the T2 such that it faces the bottom NaI detector. (b) T2 was positioned as in the experiment. It was first rotated to the position as in (a), then it was rotated clockwise about the y-axis by 45°, positioning the upstream side of the T2 such that it faces the beam right NaI detector. . . . .	43
4.1	Digital image from the OTR screen; (a) an image taken with the beam on, (b) a background image taken with the RF on but the electron gun off, (c) The background subtracted beam image ((a)-(b)). . . . .	50
4.2	Gaussian and super Gaussian fits for beam projections. The beam images is background subtracted image and taken when quadrupole magnets are turned off. Left image is Gaussian fit and right image is super Gaussian fit. . . . .	51
4.3	Square of rms values and parabolic fittings. . . . .	51

4.4	HRRL energy scan (dots) and fit (line) with two skewed Gaussian distribution.	53
4.5	The electron beam monitor.	55
4.6	The photon flux detected using scintillator. The mean of the ADC channel decreased linearly as the electron beam current was decreased.	55
4.7	Fit for accelerator beam current <i>v.s.</i> the ADC channel.	56
4.8	Photon spectrum of NaI detectors after background subtraction created by 3 MeV positrons incident on T2. (a) and (b) are spectrum after background subtractions. (c) and (d) are the spectrum of events coincident in both detectors in 511 keV peaks.	57
4.9	Positron detection using T2 and NaI detectors.	58
4.10	Photon spectrum when a permanent dipole magnet is inserted along with T2 (dashed line), dipole out and T2 in (solid line), and dipole removed and T2 out (dotted dashed line). The positron energy incident on the T2 was $2.15 \pm 0.06$ MeV.	58
4.11	The time normalized spectra of photons created by 3 MeV positrons incident on T2. In the top row are original spectrum and in the bottom row are spectrum of incidents happened in the 511 keV peak coincidentally in both detectors. The positron beam energy incident on the T2 was $3.00 \pm 0.06$ MeV.	60
4.12	The positron rates for $2.15 \pm 0.06$ MeV incident electrons measured by running NaI detectors in OR mode. The rate was 0.21 Hz for left and 0.35 Hz right NaI detectors in OR mode while the rate in coincidence (AND) mode was 0.028 Hz.	61
4.13	The ratios of positrons detected by NaI detectors in coincidence mode to the electrons impinging T1.	61
5.1	Ratio of positrons detected to electrons measured in the experiment (hollow diamond) and simulation (full circle).	64

# List of Tables

2.1	The Basic Parameters of the HRRL. . . . .	14
2.2	The HRRL Beamline Parts and Coordinates. . . . .	16
2.3	The Radioactive Sources and Corresponding Photon Peaks. . . . .	20
3.1	Predicted Number of Positrons Transported and The Number of 511 keV Photons Detected. . . . .	38
3.2	The Positron Beam Loss Along The Beamline. . . . .	40
3.3	Number of 511 keV photons observed by the NaI detectors. . . . .	42
3.4	Quadrupole Triplet System Collection and Transportation Efficiency Data. .	46
3.5	Systematic Error Study: Counts of 511 keV Photon Pairs for Different Magnet Settings. . . . .	47
4.1	Emittance Measurement Results . . . . .	52
4.2	Fit Parameters for Two Skewed Gaussian. . . . .	54
4.3	Scintillator Calibration Data. . . . .	54
4.4	Positron to Electron Rate Ratio. . . . .	59
A.1	Dipole Magnet Mapping Data. . . . .	65

# Abstract

Positrons were produced using a tungsten target when impinged by an electron beam from the High Repetition Rate Linac (HRRL) in the Physics Department's Beam Lab at Idaho State University (ISU). The produced positrons were transported to another tungsten target where they annihilate and create 511 keV photons. Two shielded NaI detectors were positioned to measure 511 keV photons in coincidence with the pulsed electron gun. The intensity of the produced positrons were measured at five (1-5 MeV) different energies using the annihilation target. The ratio of positrons detected on NaI detectors to electrons incident on T1 was on the order of  $10^{-15}$ . The ratio was the highest near 3 MeV in agreement with a simulation.

# Chapter 1

## Introduction

### 1.1 Positron Beam

Positrons are used in several disciplines of science, such as chemistry, physics, material science, surface science, biology and nanoscience [1]. Different approaches are used to generate positrons. The main challenge is increasing the intensity (or current) of the positron source. One of the most common methods used to generate a positron beam is using an electron linear accelerator (linac). The electron beam produces positrons by bremsstrahlung and pair production. One of the advantages of the linac based positron beam is its variable energy and intensity. Below are two examples that use positrons as probes.

#### 1.1.1 Positron Beam for Positron Annihilation Spectroscopy

Positron Annihilation Spectroscopy (PAS) is a non-damaging technique to detect defects in materials. PAS has become a useful method to investigate the microstructure of condensed matter and to detect small sized defects at low concentration at different depths which are hardly detectable with other traditional techniques [2]. Different depths of the materials can be probed by using a variable energy positron source such as one driven by a linac.

When positrons intercept materials, they lose energy in a process of thermalization that lowers the kinetic energy of positrons below 0.1 eV. Thermalized positrons move towards the defects within materials due to Coulomb repulsion by positive ion cores [2] where they eventually annihilate. Positrons have a longer life time in defects because of the lower electron density in the defects. Thus defect rich materials exhibit longer positron life times. One

may measure concentration and types of defects in the analyte.

### 1.1.2 Positron Beam for Measuring The Impact of Two Photon Exchange

Nucleon electromagnetic form factors are fundamental quantities that are related to the charge and magnetization distribution in the nucleon. Conventionally, the nucleon form factors are measured using the Rosenbluth Technique (RT) [3]. The form factor scaling ratio,  $R = \mu_p G_{Ep}/G_{Mp}$ , measured using this technique is around unity as shown (hollow squares) in Figure 1.1 [4]. Since the 1990's, a technique using elastic electron-proton polarization transfer to measure this ratio has been developed [4-6]. In this technique, R has been observed to decrease when the momentum transfer ( $Q^2$ ) increases, as shown (solid circles) in Figure 1.1.

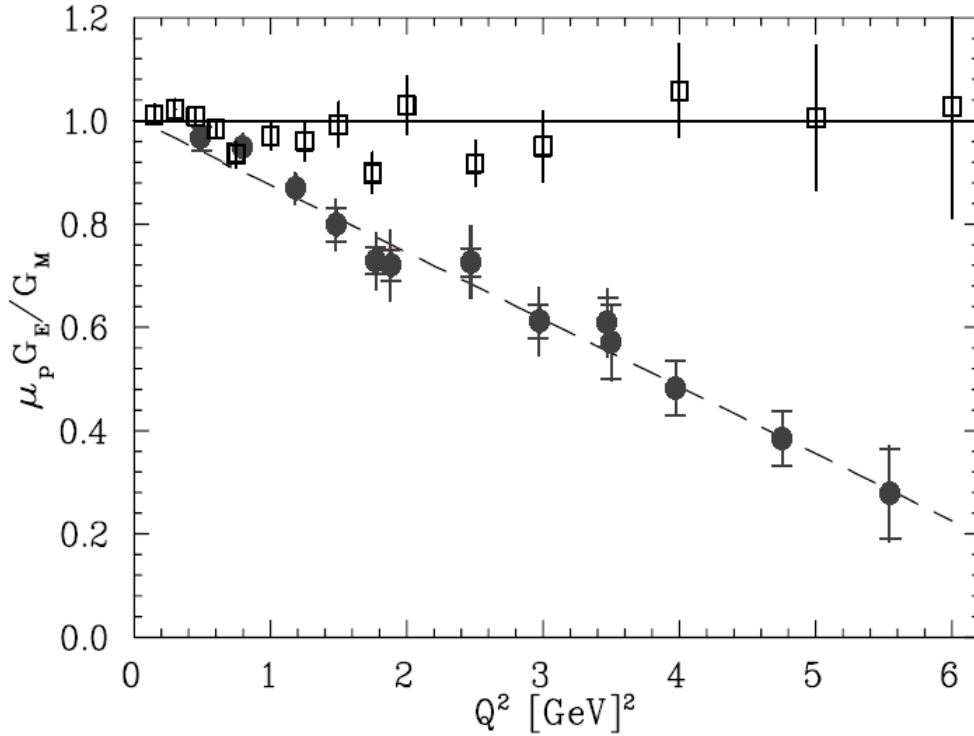


Figure 1.1: Form factor ratio (R), obtained using the Rosenbluth Technique (hollow squares) [3] and from the Recoil Polarization Technique (solid circles) [5].

The disagreement could arise from the Rosenbluth Technique's assumption that only one photon is exchanged (OPE) during the scattering while two photon exchange (TPE), which depends weakly on  $Q^2$ , could become considerable with increasing  $Q^2$  [5]. The contribution of TPE can be obtained by comparing the ratio of  $e^+ p$  to  $e^- p$  scattering. The interference of OPE and TPE can also be studied in the scattering process  $e^+e^- \rightarrow p\bar{p}$  [7].

## 1.2 Positron Beam Generation from Bremsstrahlung

When a moving charged particle interacts with the electric field of another charged particle, it can be deflected and lose energy in the form of photons, as shown in Figure 1.2. This interaction is known as the bremsstrahlung process. The probability of this interaction increases with the square of the atomic number of the material traversed by the incident charged particle. Figure 1.3 shows the photon energy distribution produced when the 12 MeV electron energy distribution from Figure 1.4 interacts with a 1 mm thick tungsten target. As shown in Figure 1.3, the distribution peaks at 0.3 MeV.

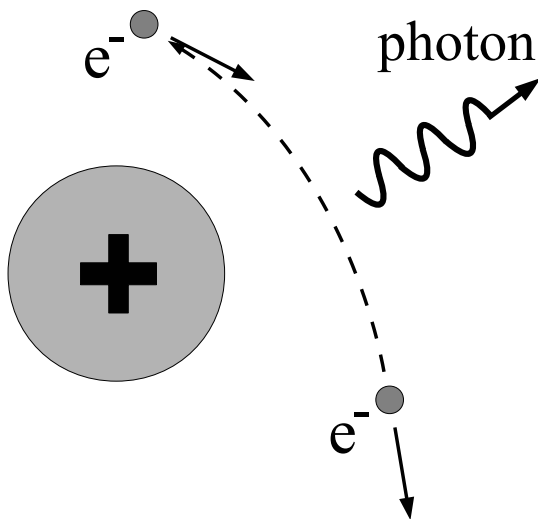


Figure 1.2: Photon emission from the bremsstrahlung processes.

The bremsstrahlung cross section given is by [8]

$$d\sigma = 4Z^2 r_e^2 \alpha \frac{d\nu}{\nu} \left\{ \left( 1 + \left( \frac{E}{E_0} \right)^2 \right) \left[ \frac{\phi_1(\gamma)}{4} - \frac{1}{3} \ln Z - f(Z) \right] - \frac{2E}{3E_0} \left[ \frac{\phi_2(\gamma)}{4} - \frac{1}{3} \ln Z - f(Z) \right] \right\}, \quad (1.1)$$

where  $E_0$  is initial total energy of the electron,  $E$  is the final total energy of the electron,  $\nu = \frac{E_0 - E}{h}$  is frequency of the emitted photon, and  $Z$  is atomic number of the target.  $\gamma = \frac{100m_e c^2 h\nu}{E_0 E Z^{1/3}}$  is the charge screening parameter, and  $f(Z)$  is given by

$$f(Z) = (Z\alpha)^2 \sum_1^{\infty} \frac{1}{n[n^2 + (Z\alpha)^2]}, \quad (1.2)$$

where  $\alpha = \frac{1}{137}$  is the fine-structure constant,  $\phi_1$  and  $\phi_2$  are screening functions that depend on  $Z$ .

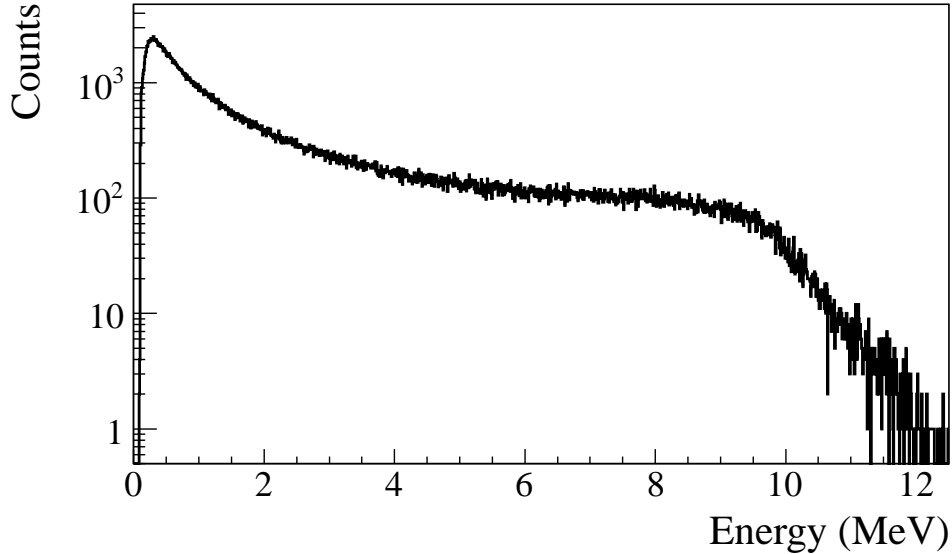


Figure 1.3: Bremsstrahlung photon energy distribution produced when the 12 MeV electron energy distribution from Figure 1.4 interacts with the simulation's 1 mm thick tungsten target.



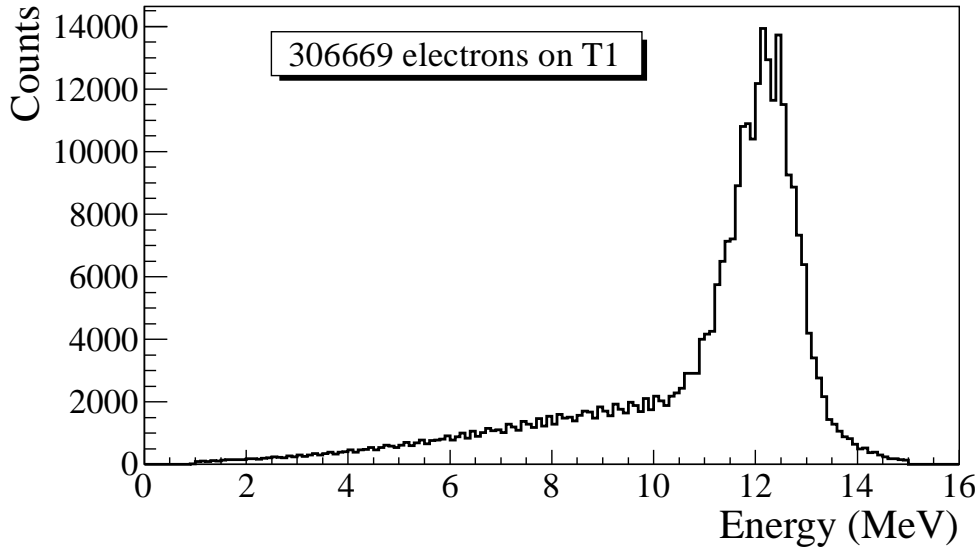


Figure 1.4: The electron energy distribution incident on a tungsten foil in simulation.

There are three competing processes that a photon can undergo when interacting with matter. Figure 1.5 illustrates the cross-sections for different interactions that can occur when a photon traverses tungsten as a function of photon energy. At electron volt (eV) energies, which are comparable to the electron atomic binding energy, the dominant photon interaction is the photoelectric effect. As the photon energy increases up to the kilo electron volt (keV) range, the Compton scattering process starts to be more dominant. Although the photon is totally absorbed during the photoelectric effect, photons merely lose energy when undergoing Compton scattering. As the photon energy reaches twice the rest mass energy of the electron, *i.e.*  $2 \times 511$  keV, pair production begins to occur. Pair production becomes the dominant interaction process when photon energies are beyond 5 MeV [9]. In this process, a photon interacts with the electric field of the nucleus or the bound electrons and is converted into an electron and positron pair.

Using natural units, where  $c \equiv 1$ , the differential cross-section for pair production can be

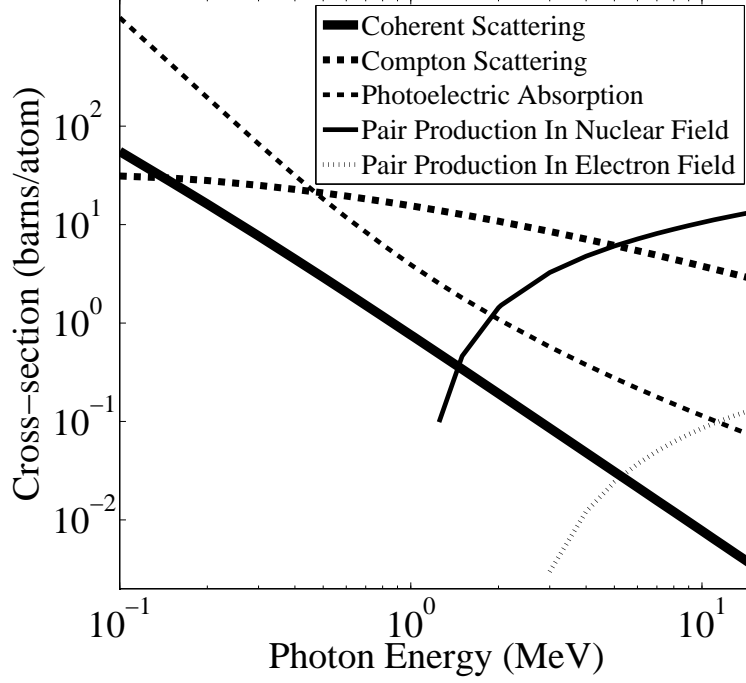


Figure 1.5: The cross-sections for different types of photon interactions with tungsten as a function of photon energy [10].

expressed as

$$\begin{aligned}
\frac{d\sigma}{d\epsilon_1 d\theta_1 d\theta_2} &= 8 \left( \frac{\pi a}{\sinh(\pi a)} \right)^2 \frac{a^2 e^2}{2\pi \hbar c} \left( \frac{\hbar}{m_e c} \right)^2 \frac{\epsilon_1 \epsilon_2}{k^3} \theta_1 \theta_2 \\
&\times \left\{ \frac{V^2(x)}{q^4} [k^2(u^2 + v^2)\xi\eta - 2\epsilon_1\epsilon_2(u^2\xi^2 + v^2\eta^2) + 2(\epsilon_1^2 + \epsilon_2^2)uv\xi\eta\cos(\phi)] \right. \\
&\quad \left. + a^2 W^2(x)\xi^2\eta^2 [k^2(1 - (u^2 + v^2)\xi\eta - 2\epsilon_1\epsilon_2(u^2\xi^2 + v^2\eta^2) - 2(\epsilon_1^2 + \epsilon_2^2)uv\xi\eta\cos(\phi))] \right\}, \tag{1.3}
\end{aligned}$$

where  $k$  is photon energy,  $\theta_1$  and  $\theta_2$  are the scattering angle of  $e^+$  and  $e^-$  respectively,  $\phi = \phi_1 - \phi_2$  is the angle between the  $e^+$  and  $e^-$  pair,  $\epsilon_1$  and  $\epsilon_2$  are the energy of the positron and electron respectively. Other constants are  $u = \epsilon_1\theta_1$ ,  $v = \epsilon_2\theta_2$ ,  $\xi = \frac{1}{1+u^2}$ ,  $\eta = \frac{1}{1+v^2}$ ,  $q^2 = u^2 + v^2 + 2uv\cos(\phi)$ ,  $x = 1 - q^2\xi\eta$ ,  $a = \frac{Ze^2}{\hbar c}$ ,  $V(x) = 1 + \frac{a^2}{(1!)^2} + \frac{a^2(1+a^2)x^2}{(2!)^2} + \frac{a^2(1+a^2)(2^2+a^2)x^4}{(3!)^2} + \dots$ , and  $W(x) = \frac{1}{a^2} \frac{dV(x)}{dx}$ .

In pair production, positron and electron pairs are created back to back in the center

of mass frame. In the lab frame, electrons and positrons tend to move in the direction of the photon, as shown in Figure 1.6. The positron and electron carry away the energy from the photon that is in excess of 1.022 MeV. In the center of mass frame, the kinetic energy is equally shared. Photons with an energy above 1.022 MeV in the bremsstrahlung spectrum of Figure 1.3 have the potential to create electron and positron pairs. Figure 1.7 is the simulation of 10 million 12 MeV mono energetic electrons impinging on a 1.016 mm thick tungsten target. Turning on the annihilation process resulted in a 511 keV peak on top of the bremsstrahlung spectrum. This 511 keV peak represents photons produced when the created positrons from the pair production annihilate with atomic electrons inside the tungsten target.

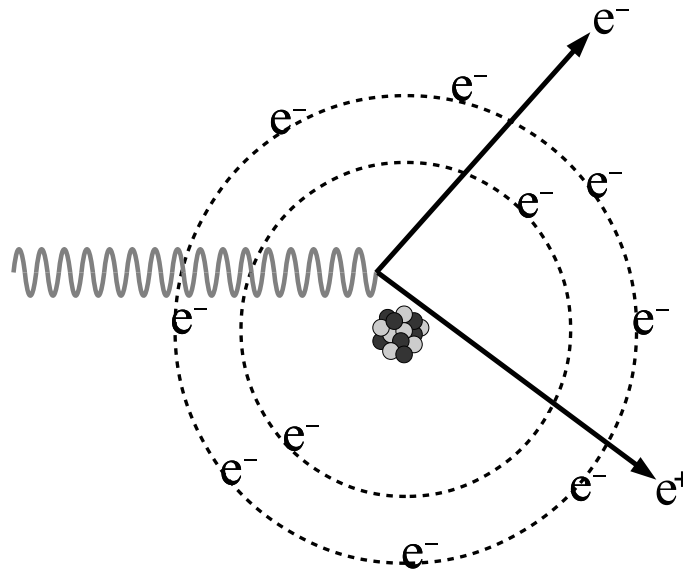


Figure 1.6: Pair production.

### 1.3 Emittance Measurement

When the emittance and Twiss parameters are given at the exit of a linac, one will be able to calculate the beam size and the divergence at any given point along the beamline.

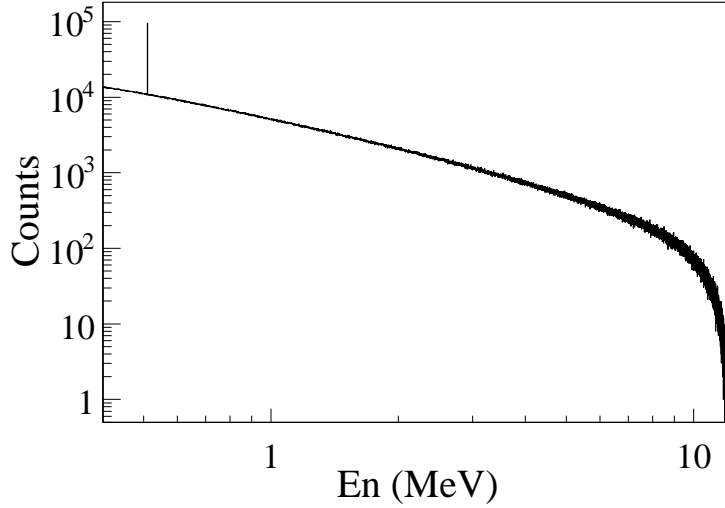


Figure 1.7: Photon spectrum of created by million 12 MeV mono energy electrons impinging on a 1.016 mm thick tungsten target.

To optimized positron production, one needs to know the beam size and divergence on the production target. Emittance and Twiss parameters are the input parameters for any accelerator simulation tools used to study beam transport and make predictions of the beam properties along the beam line.

### 1.3.1 Emittance

In accelerator physics, a Cartesian coordinate system is used to describe the motion of the accelerated particles. As shown in Figure 1.8, the  $s$ -axis of the Cartesian coordinate system is defined as the natural coordinate that is oriented along the same direction as the beam momentum. The  $x$ -axis and  $y$ -axis are horizontal and vertical coordinates which constitute the transverse beam profile. The transverse beam profiles are described as a function of the longitudinal coordinates,  $x(s)$  and  $y(s)$ .

The phase space  $x'$  vs.  $x$  of the beam is an ellipse with invariant area (along the beamline).

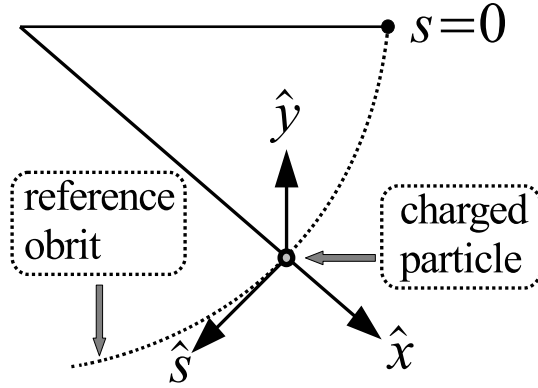


Figure 1.8: Coordinated system and reference orbit (dashed line) [11].

Here  $x'$  is defined as

$$x' = \frac{dx}{ds}. \quad (1.4)$$

This invariant is called the Courant-Snyder invariant [11]. The transverse emittance  $\epsilon$  of the beam is defined to be the area of the ellipse that contains 90% of the particles. Beam divergence and Twiss parameters are related to the beam size and divergence by

$$\sigma_x(s) = \sqrt{\epsilon_x(s)\beta_x(s)}, \quad \sigma_{x'}(s) = \sqrt{\epsilon_x(s)\gamma_x(s)}, \quad (1.5)$$

where  $\epsilon_x$  is beam's horizontal emittance,  $\sigma_x$  is the beam size's rms,  $\sigma_{x'}$  is the beam divergence's rms, and  $\beta_x$  and  $\gamma_x$  are two of the three Twiss parameters.

### 1.3.2 Emittance Measurement

The HRRL beam emittance was measured using optical transition radiation (OTR). This transition radiation was theoretically predicted by Ginzburg and Frank [12] in 1946 to occur when a charged particle passes the boundary of two media. An OTR based viewer was installed to observe the electron beam size at 37.2 mA electron peak currents, available

using the HRRL at 15 MeV with 200 ns macro pulse width. The visible light is produced when a relativistic electron beam crosses the boundary of two media with different dielectric constants.

Light is emitted in a conical shape at backward angles with the peak intensity at an apex angle of  $\theta = 1/\gamma$  with respect to the incident electron's angle of reflection. A 15 MeV electron accelerated by the HRRL would emit light at  $\theta = 2^\circ$ . Orienting the OTR target at  $45^\circ$  with respect to the incident electron beam will result in the high intensity photons being observed at an angle of  $90^\circ$  with respect to the incident beam, see Figure 1.9. These backward-emitted photons are observed using a digital camera and can be used to measure the shape and the intensity of the electron beam based on the OTR distribution. Although an emittance measurement can be performed in several ways [13, 14], the quadrupole scanning method [15] was used to measure the emittance and Twiss parameters in this work.

### 1.3.3 Quadrupole Scanning Method

Fig. 1.9 illustrates the beamline components used to measure the emittance for the quadrupole scanning method. A quadrupole is positioned at the exit of the linac to focus or de-focus the beam as observed on the OTR view screen. The 3.1 m distance between the quadrupole and the screen was chosen in order to minimize chromatic effects and to satisfy the thin lens approximation. Assuming the thin lens approximation,  $\sqrt{k_1}L \ll 1$ , is satisfied, the transfer matrix of a quadrupole magnet may be expressed as

$$\mathbf{Q} = \begin{pmatrix} 1 & 0 \\ -k_1L & 1 \end{pmatrix} = \begin{pmatrix} 1 & 0 \\ -\frac{1}{f} & 1 \end{pmatrix}, \quad (1.6)$$

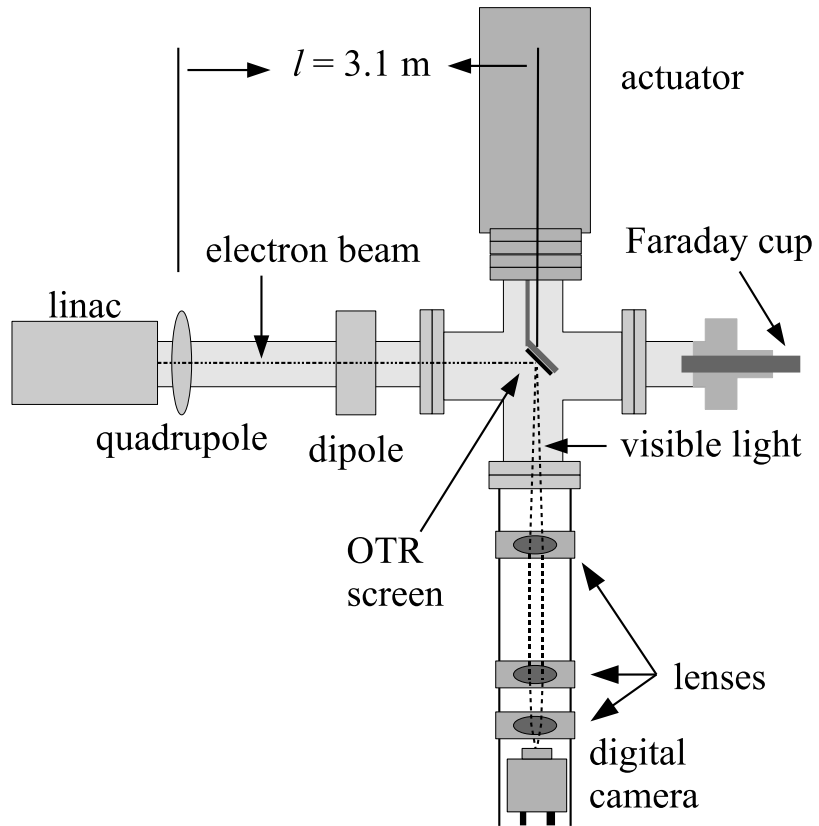


Figure 1.9: Apparatus used to measure the beam emittance.

where  $k_1$  is the quadrupole strength,  $L$  is the length of quadrupole, and  $f$  is the focal length. A matrix representing the drift space between the quadrupole and screen is given by

$$\mathbf{S} = \begin{pmatrix} 1 & l \\ 0 & 1 \end{pmatrix}, \quad (1.7)$$

where  $l$  is the distance between the scanning quadrupole and the screen. The transfer matrix  $\mathbf{M}$  of the scanning region is given by the matrix product  $\mathbf{S}\mathbf{Q}$ . In the horizontal plane, the beam matrix at the screen ( $\sigma_s$ ) is related to the beam matrix of the quadrupole ( $\sigma_q$ ) using the similarity transformation

$$\sigma_s = \mathbf{M}\sigma_q\mathbf{M}^T. \quad (1.8)$$

where the  $\sigma_s$  and  $\sigma_q$  are defined as [16]

$$\sigma_{s,x} = \begin{pmatrix} \sigma_{s,x}^2 & \sigma_{s,xx'} \\ \sigma_{s,xx'} & \sigma_{s,x'}^2 \end{pmatrix}, \quad \sigma_{q,x} = \begin{pmatrix} \sigma_{q,x}^2 & \sigma_{q,xx'} \\ \sigma_{q,xx'} & \sigma_{q,x'}^2 \end{pmatrix}. \quad (1.9)$$

By defining the new parameters [15]

$$A \equiv l^2 \sigma_{q,x}^2, \quad B \equiv \frac{1}{l} + \frac{\sigma_{q,xx'}}{\sigma_{q,x}^2}, \quad \text{and} \quad C \equiv l^2 \frac{\epsilon_x^2}{\sigma_{q,x}^2}, \quad (1.10)$$

the matrix element  $\sigma_{s,x}^2$ , the square of the beam size's rms at the screen, may be expressed as a parabolic function of the product of  $k_1$  and  $L$

$$\sigma_{s,x}^2 = A(k_1L)^2 - 2AB(k_1L) + (C + AB^2). \quad (1.11)$$

The emittance measurement was performed by changing the quadrupole current, which changes  $k_1L$ , and measuring the corresponding beam image size on the view screen. The measured two-dimensional beam image was projected along the image's abscissa and ordinate



axes. A Gaussian fitting function is used on each projection to determine the rms value,  $\sigma_s$  in Eq. (1.11). Measurements of  $\sigma_s$  for several quadrupole currents ( $k_1L$ ) are then fit using the parabolic function in Eq. (1.11) to determine the constants  $A$ ,  $B$ , and  $C$ . The emittance ( $\epsilon$ ) and the Twiss parameters ( $\alpha$  and  $\beta$ ) can be found using Eq. (1.12)

$$\epsilon = \frac{\sqrt{AC}}{l^2}, \quad \beta = \sqrt{\frac{A}{C}}, \quad \alpha = \sqrt{\frac{A}{C}}\left(B + \frac{1}{l}\right). \quad (1.12)$$

# Chapter 2

## Apparatus

### 2.1 HRRL Beamline

A 16 MeV S-band (2856 MHz RF frequency) High Repetition Rate Linac (HRRL) located in the Department of Physics Beam Lab at Idaho State University is used to impinge a 12 MeV electron beam onto a tungsten foil. The energy of the HRRL is tunable between 3 to 16 MeV and its repetition rate variable from 1 to 300 Hz. The operating range of the HRRL is given in Table 2.1. As shown in Figure 2.1, the HRRL has a thermionic gun, vertical and horizontal steering magnet sets on two ends, and two solenoid magnets.

The accelerator's cavity was relocated to the position shown in Figure 2.2 to provide enough space for a beam line that can transport either positrons or electrons. The beam elements are described in Table 2.2. Quadrupole and dipole magnets were added to the new beam line as well as diagnostic tools like an OTR and YAG screens. Faraday cups and toroids were installed to measure the electron beam size and the current. Energy slits were installed to control the energy/momentum spread of the beam after the first dipole. A 1.016 mm thick retractable tungsten foil target (T1) was placed between the 1st and 2nd

Table 2.1: The Basic Parameters of the HRRL.

Parameter	Unit	Value
maximum energy	MeV	16
peak current	mA	100
repetition rate	Hz	300
absolute energy spread	MeV	2-4
macro pulse length	ns	>50

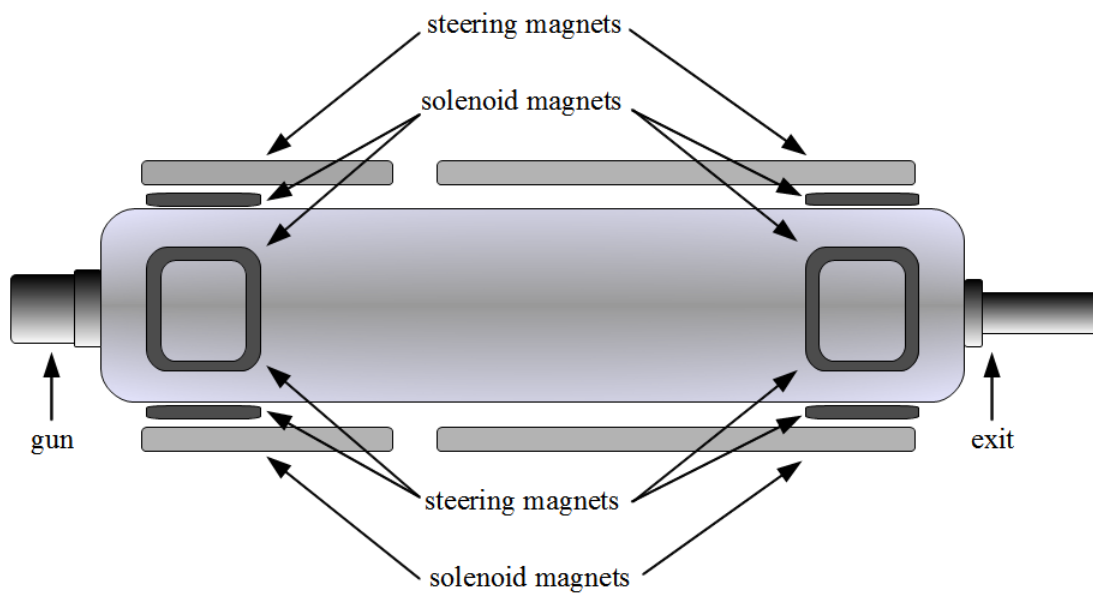


Figure 2.1: The configuration of the HRRL cavity.

Table 2.2: The HRRL Beamline Parts and Coordinates.

Label	Beamline Element	Distance from Linac Exit (mm)
Q1	quadrupole	335
Q2	quadrupole	575
Q3	quadrupole	813
T1	e <sup>+</sup> production target	1204
Q4	quadrupole	1763
Q5	quadrupole	2013
Q6	quadrupole	2250
D1	dipole	2680
S1	OTR screen	3570
FC1	Faraday cup	3740
EnS	energy slit	3050
S2	YAG screen	3410
Q7	quadrupole	3275
D2	dipole	3842
FC2	Faraday cup	4142
Q8	quadrupole	4044
Q9	quadrupole	4281
Q10	quadrupole	4571
T2	annihilation target	7381

quadrupole triplets and used to produce positrons when the electron beam interacts with it. The room where the HRRL is located is divided by a wall into two parts; the accelerator side and the experimental cell. A beam pipe at the end of the 90 degree beamline goes through a hole in the wall and delivers the beam from the accelerator side to the experimental cell. The positron detection system consisting of two NaI detectors was placed at the end of the beamline in the experimental cell side as shown in Figure 2.2.

## 2.2 The OTR Imaging System

The OTR target is a 10  $\mu\text{m}$  thick aluminum foil with a 1.25 inch diameter. The OTR is emitted in a cone shape with the maximum intensity at an angle of  $1/\gamma$  with respect to

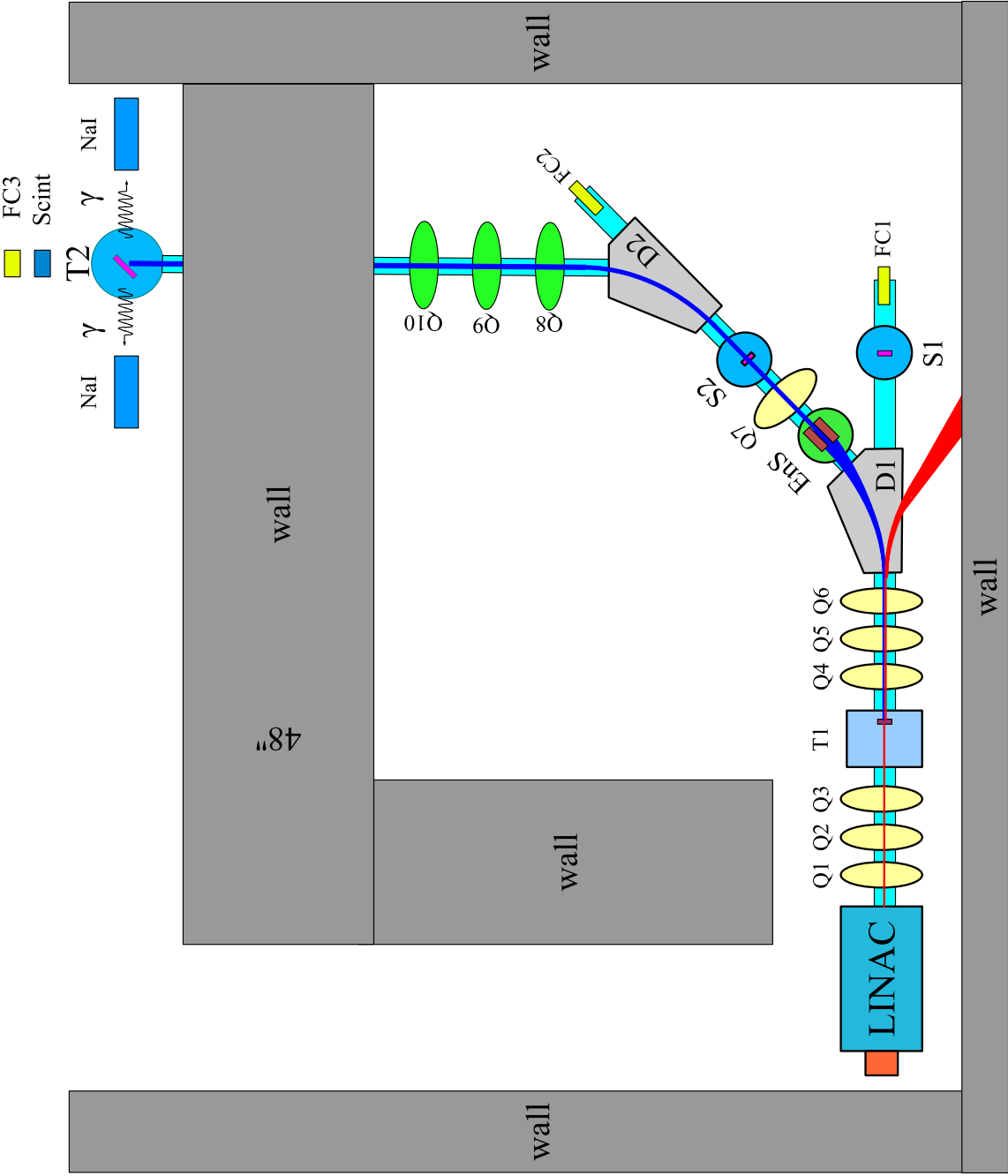


Figure 2.2: The HRRL beamline layout and parts.

the reflecting angle of the electron beam [17]. Three two inch diameter lenses are used for the imaging system to avoid optical distortion at lower electron energies. The focal lengths and positions of the lenses are shown in Figure 2.3. The camera used is a JAI CV-A10GE digital camera with a 767 by 576 pixel area. The images were taken by triggering the camera synchronously with the electron gun.

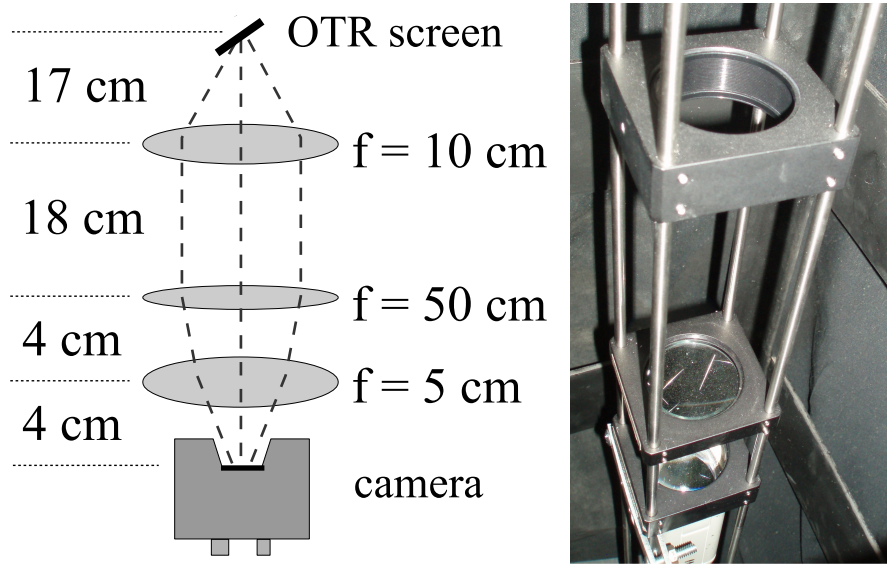


Figure 2.3: The OTR imaging system.

## 2.3 Positron Detection

When the electron beam is incident on T1, photons and secondary electrons are created along with positrons. These particles are the main source of noise in the experiment. The positrons were transported to the second tungsten target (T2) which was shielded from this noise by the concrete wall and Pb bricks. The setup is shown in Figure 2.4. A 6-way cross was placed at the end of the beamline to hold T2. The 6-way cross has three 1 mil (0.0254 millimeters) thick stainless steel windows. The two horizontal windows perpendicular to the beamline allowed the 511 keV photons created from the positron annihilation to escape the beamline with limited attenuation. A third window at the end of the 90 degree beamline

was used as the beam exit. Two NaI detectors were placed facing the two exit windows to detect the photons produced in T2. A two inch thick lead brick collimator with a 2 inch diameter hole was placed between the exit window and NaI detector. A scintillator (Scint) and a Faraday cup (FC3) were placed at the end of the beamline and were used to tune the electron and positron beam. When positrons reach T2, they can thermalize and annihilate inside T2. During thermalization, a positron loses its kinetic energy. When it annihilates with an electron, two 511 keV photons are emitted back to back. A triplet coincidence is required between the accelerator RF pulse and the detection of a photon in each NaI detector.

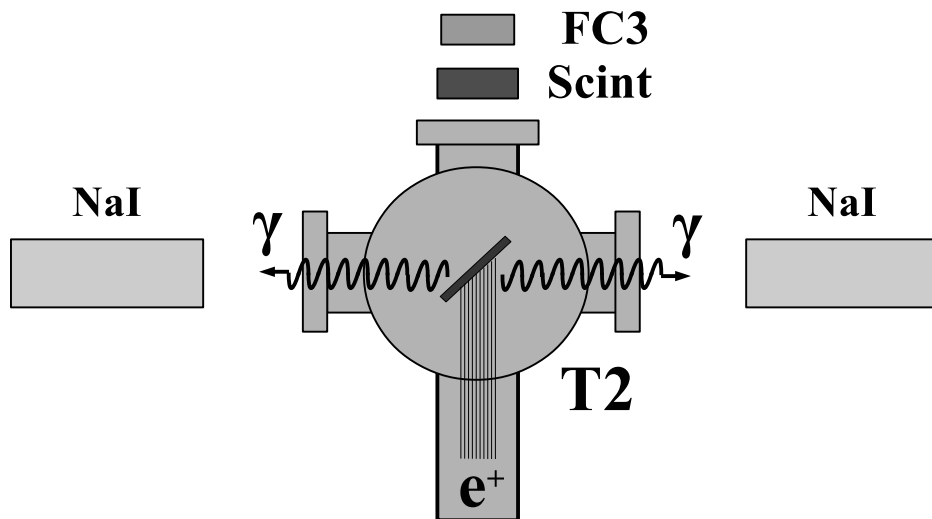


Figure 2.4: The positron detection system: T2 (pink) was placed with  $45^\circ$  angle to the horizontal plane first, then rotated  $45^\circ$  along the vertical axis.

### 2.3.1 NaI Detectors

NaI crystals, shown in Figure 2.5, were used to detect 511 keV photons from positron annihilation. Originally, the detectors had pulse signal lengths around  $400 \mu s$ . New PMT bases were built to use the HV divider shown in Figure 2.6. A picture of the constructed bases is shown in Figure 2.7. The pulse length of the new PMT bases is about  $1 \mu s$ . The

Table 2.3: The Radioactive Sources and Corresponding Photon Peaks.

Radioactive Sources	Unit	First Peak	Second Peak
Co-60	keV	1173	1332
Na-22	keV	511	1275

NaI crystal is from Saint-Gobain Crystal & Detectors (Mod. 3M3/3) with a dimension of  $3'' \times 3''$ . The operating high voltage of -1150 V would position the 511 keV photons within the range of the charge sensing ADC (CAEN Mod. V792).

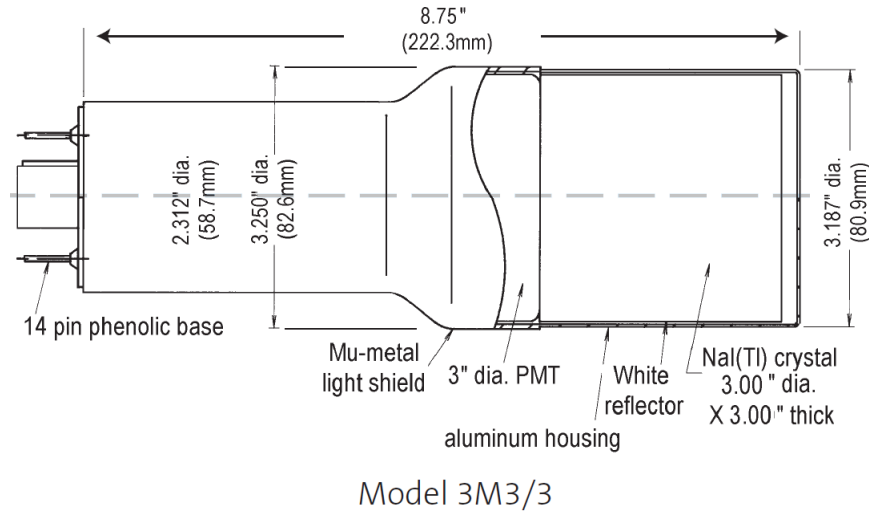


Figure 2.5: The NaI crystal dimension.

The NaI detectors were calibrated using a Na-22 and a Co-60 source with the photon peaks indicated in Table 2.3. Figure 2.8 is the oscilloscope image of several Co-60 photon pulses observed by the detector with the new PMT. The calibrated NaI detector spectrum from the Na-22 and Co-60 sources is shown in Figure 2.9. The rms values of the fits on the four peaks shown in Figure 2.9 are  $\sigma_{Na,511} = 18.28 \pm 0.04$  keV,  $\sigma_{Na,1275} = 44.51 \pm 0.27$  keV,  $\sigma_{Co,1173} = 42.49 \pm 0.24$  keV, and  $\sigma_{Co,1332} = 50.30 \pm 0.39$  keV.

The Na-22 source was placed between two NaI detectors to measure the spectrum when the RF was on, represented by dotted line (no electrons were fired from accelerator gun), and off, represented by dashed line in Fig 2.10. The solid line in Fig 2.10 represents the photon



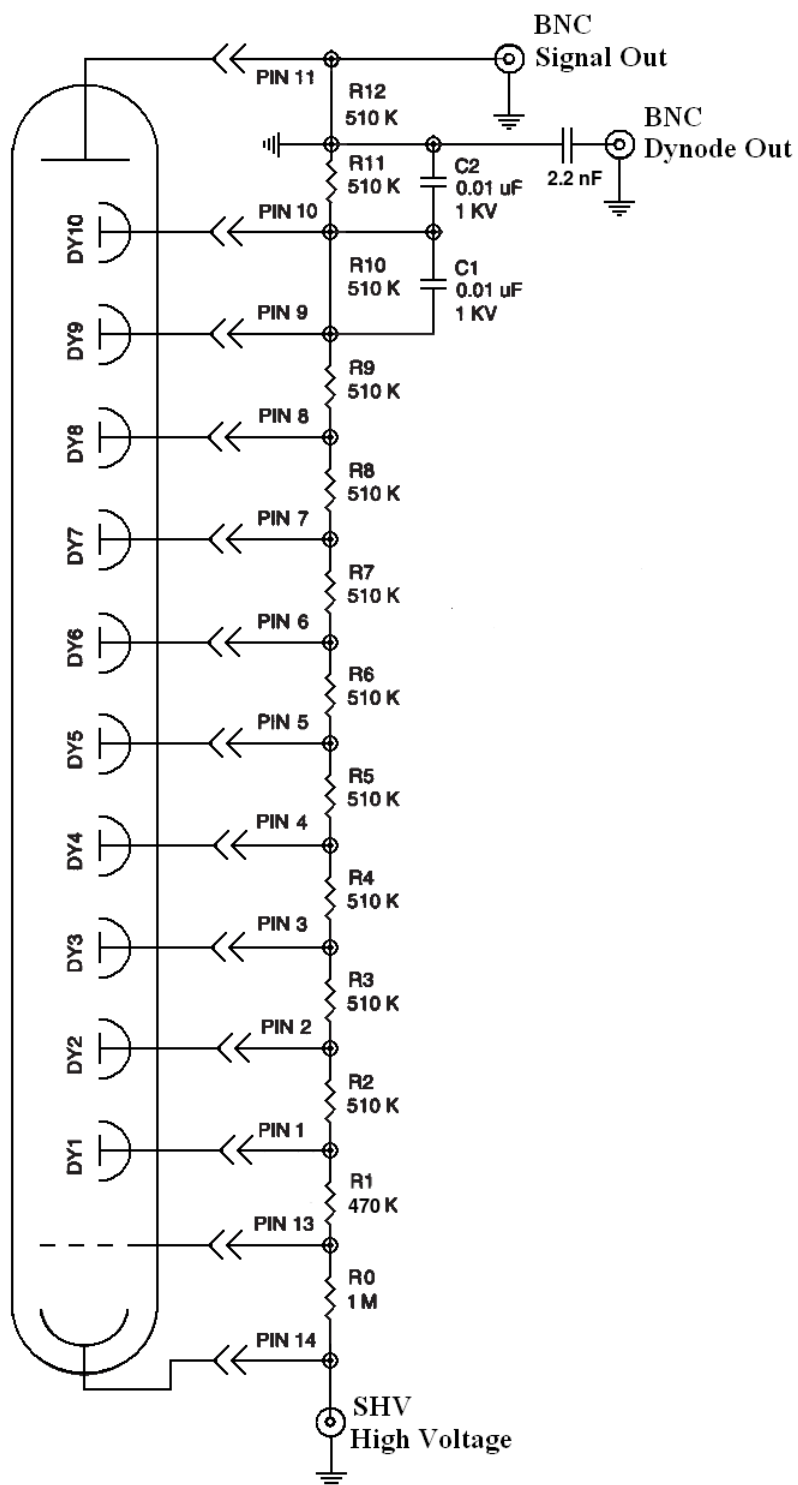


Figure 2.6: The modified PMT base design.



Figure 2.7: The NaI crystals and new bases.

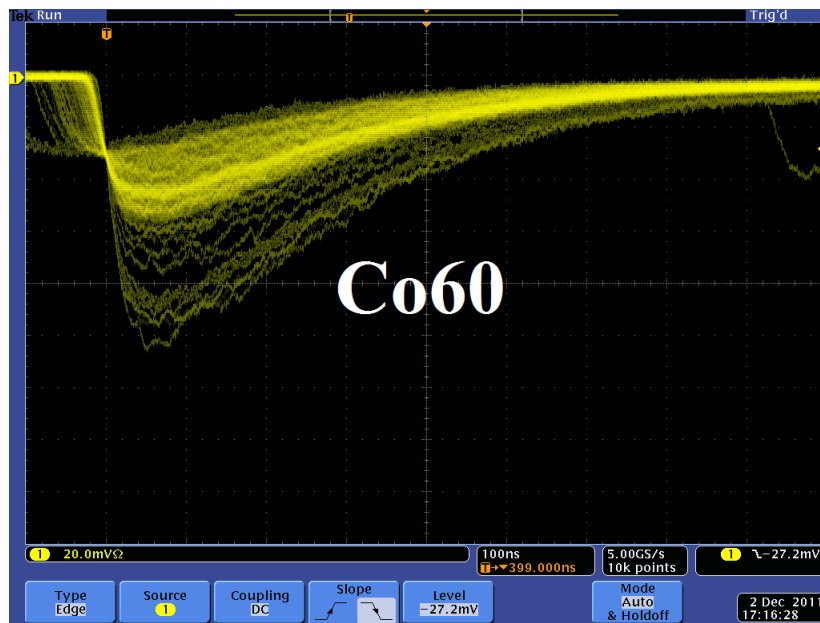


Figure 2.8: Detector output pulses using the Co-60 source and new PMT. The amplitude of the pulse is about 60 mV. The rise time of the pulse is larger than 50 ns, and the fall time is larger than 700 ns.

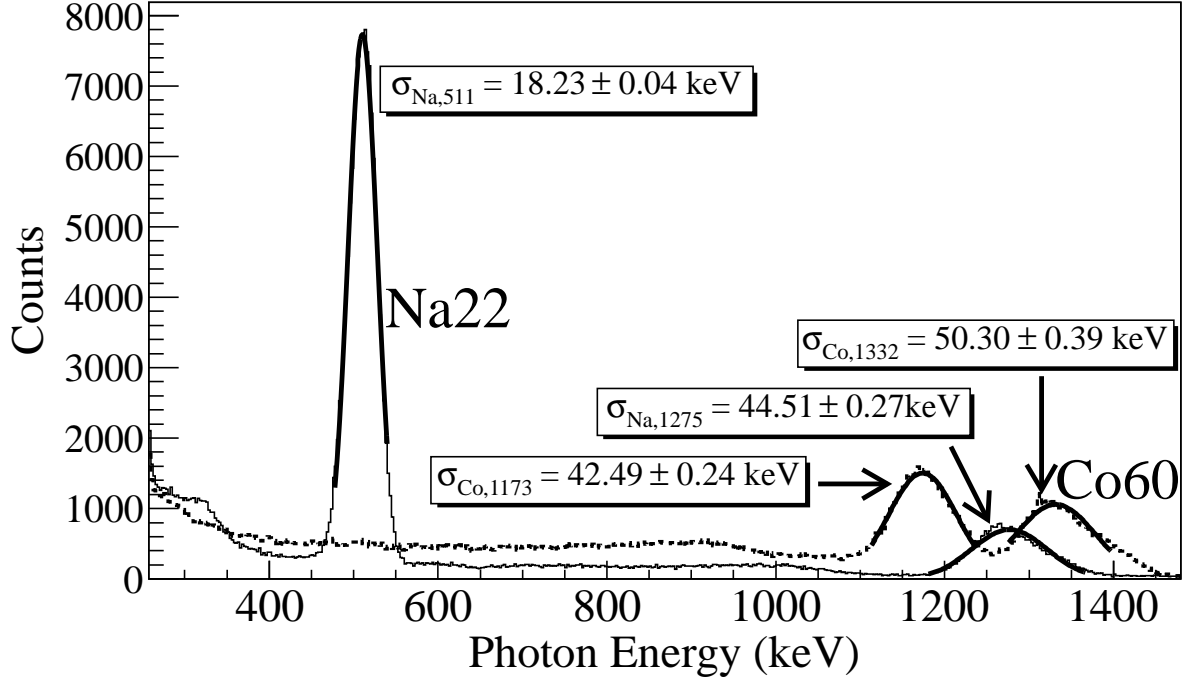
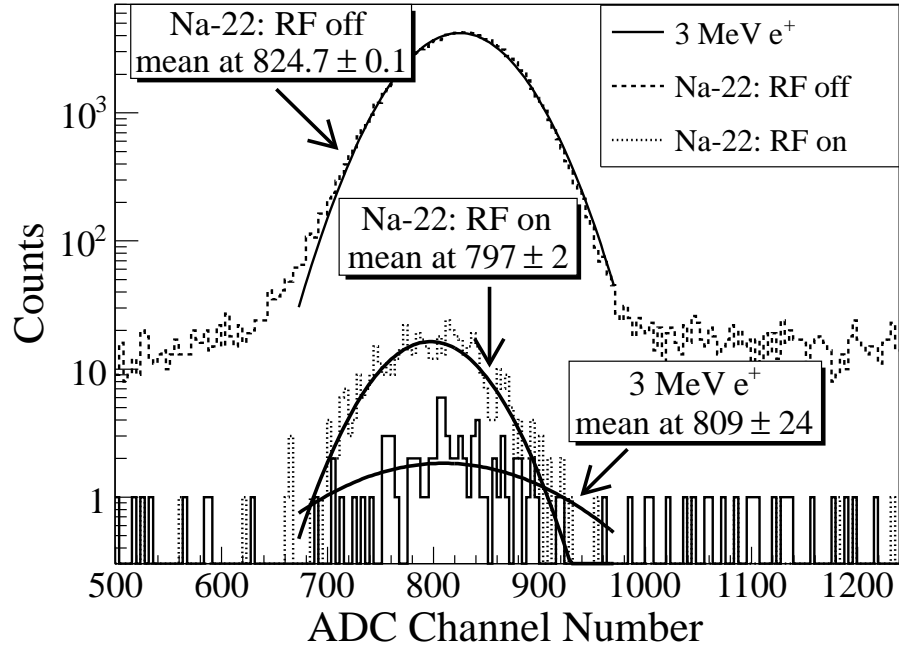


Figure 2.9: The calibrated NaI spectrum of Na-22 and Co-60 sources.

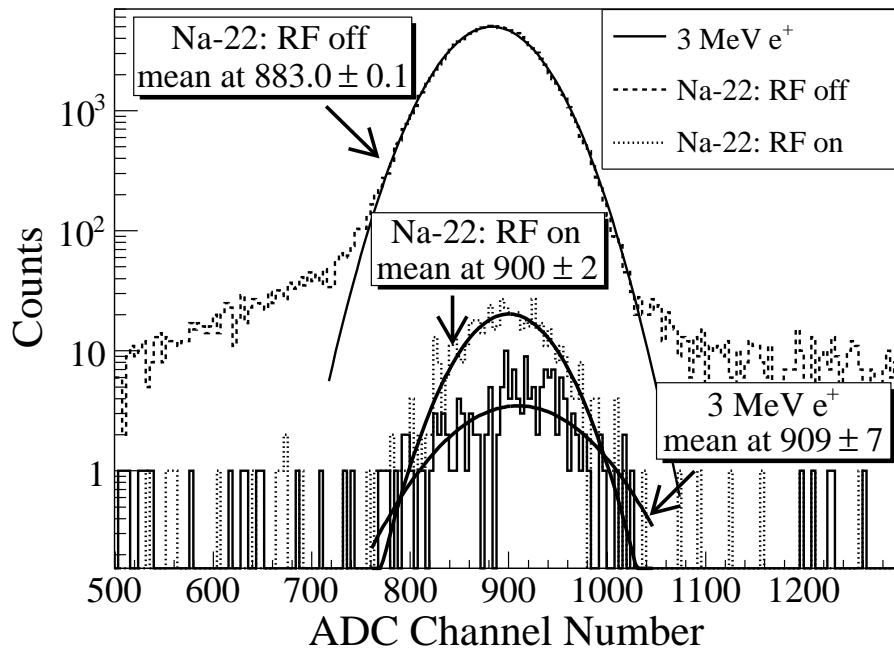
spectrum created by 3 MeV positrons impinging on T2. The 511 keV peak in the right NaI detector was shifted to the right side of the spectrum by 17 channels when the RF was on as shown in Figure 2.10 (a) while in the left NaI detector the peak shifted to the left by 28 channels as shown if Figure 2.10 (b). When the RF was on, no difference was observed for photon peaks created by Na-22 source and 3 MeV positrons. The photon peak created by Na-22 source shifted when the RF was off.

### 2.3.2 The DAQ Setup

The data acquisition (DAQ) setup and timing diagram is shown in Figure 2.11. The last dynode signals from left and right NaI detectors were inverted using a ORTEC 474 inverting amplifier and sent to an CAEN Mod. N842 constant fraction discriminator (CFD). An electron gun pulse generated VETO sent to CFD prevented the RF noise from triggering the CFD. The CFD generated multiple digital pulses for a single signal received. A GG



(a) Left NaI detector.



(b) Right NaI detector.

Figure 2.10: The 511 keV peak observed using NaI detectors shifted when accelerator RF was on. The spectrum were taken with RF on (dotted line) and with RF off (dashed line). The solid line represents the photon spectrum created by 3 MeV positrons impinging on T2.

8000-01 octal gate generator was used to create a single  $1 \mu\text{s}$  wide pulse from the first pulse in order to ignore the multiple CFD pulses produced by a single analog output pulse from the detector. The coincidence was formed between the gun pulse and the  $1 \mu\text{s}$  wide pulse from each detector using a LeCroy model 622 logic module as given by

$$\text{NaI Left} \ \&\& \ \text{NaI Right} \ \&\& \ \text{Gun Trigger}. \quad (2.1)$$

The ADC requires  $5.7 \mu\text{s}$  to convert the analog signal to a digital signal. The logic module output was delayed  $6 \mu\text{s}$  by a dual timer (CAEN Mod. N93B) to accommodate the ADC's conversion time and trigger the DAQ. The ADC (CAEN Mod. V792) converted the NaI detector's analog signals to digital when a  $1 \mu\text{s}$  gate created by gun pulse using a dual timer was present as shown in the lower part of Figure 2.11. The ADC was fast cleared unless a veto signal created using a dual timer was received from the inverted output of logic module.

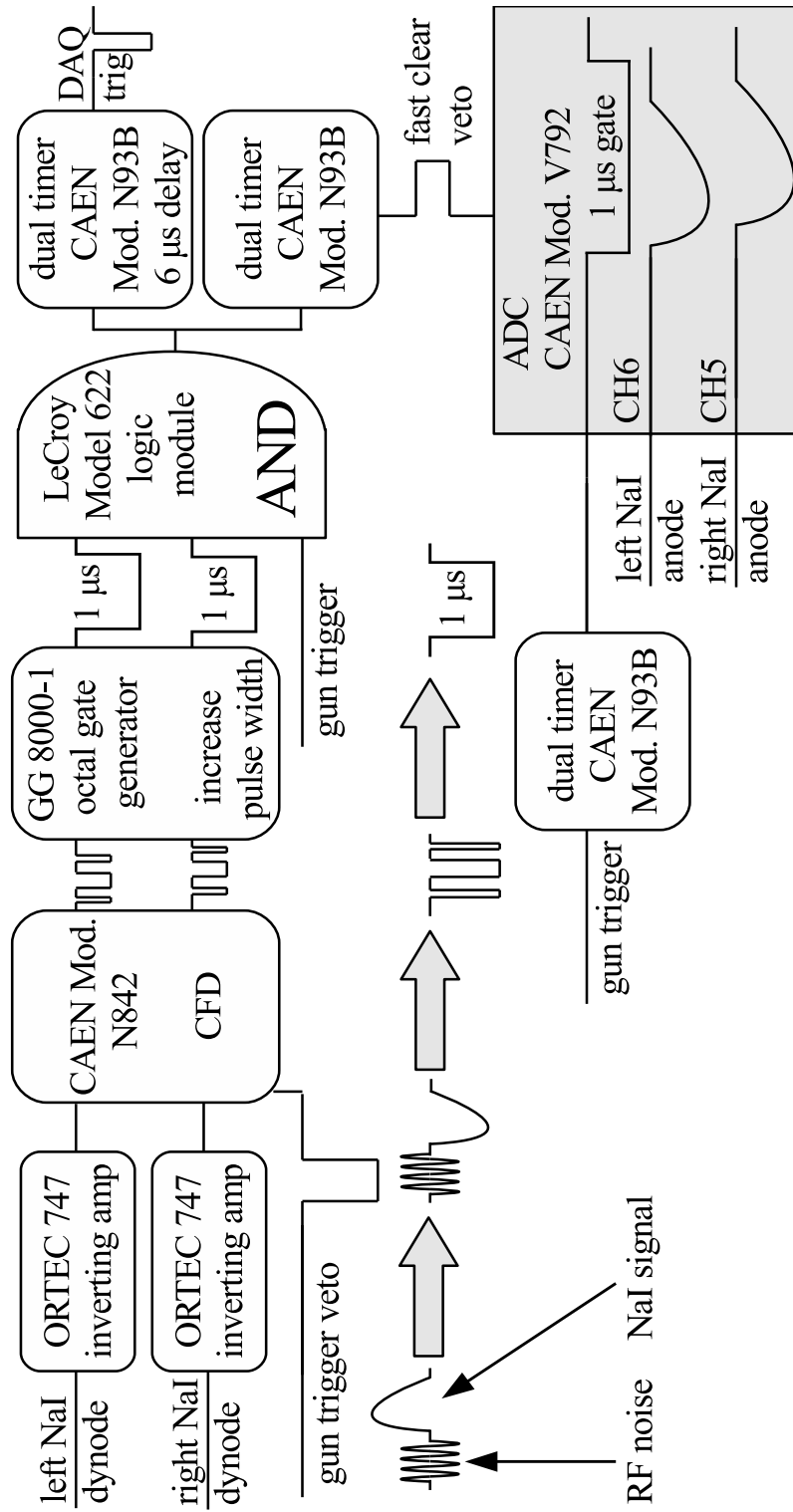


Figure 2.11: The DAQ setup and timing diagram.

# Chapter 3

## Simulation

Simulations were performed using G4beamline [18] to study the processes of position generation and transportation. “G4beamline is a particle tracking and simulation program based on the GEANT4 [19] toolkit that is specifically designed to easily simulate beamlines and other systems using single-particle tracking [18].” The simulation predicts that at least one positron is created per 1000 incident 10 MeV electrons. A large amount of beam loss was observed during the initial simulation. As a result, the simulation was divided into three steps based on the locations along the beamline that saw more than 90% beam loss. A new beam event generator was created based on the results of the previous step in the simulation.

The first step generated an electron beam with the energy distribution that was observed in the experiment shown in Figure 4.4. The electrons were focused by three quadrupoles onto the target T1, see Figure 2.2. Electrons transversing T1 produced bremsstrahlung photons of sufficient energy to produce  $e^+e^-$  pairs. The second step simulated the transportation of positrons exiting T1 to the entrance of the first dipole D1. The third step transported positrons from the entrance of D1 to the annihilation target T2, the interactions of positrons with T2, and the detection of the resulting 511 keV photon pairs.

### 3.1 Step 1 - The Electron Beam Generation and Transportation to T1

In the first simulation step, an electron beam was generated with an energy distribution that was observed in the experiment. The emittance, the Twiss parameters, and the energy

distribution of the electron beam were measured experimentally and used to generate the electron beam. The energy distribution of the electron beam is shown in Figure 4.4. The distribution was fit using two skewed Gaussian distributions. The fit parameters given in Table 4.2 were used to generate electrons.

A series of virtual detectors were placed along the beamline to sample the beam. As an example, three virtual circular detectors and T1 are shown in Figure 3.1. The electron beam was detected by a virtual detector DUPT1 (Detector UPstream of T1) placed 25.52 mm upstream of T1. Positrons, electrons, and photons generated during the interaction of the electron beam with T1 were observed by virtual detectors DT1 (Detector of T1) and DDNT1 (Detector Downstream of T1) placed 25.52 mm downstream of T1.

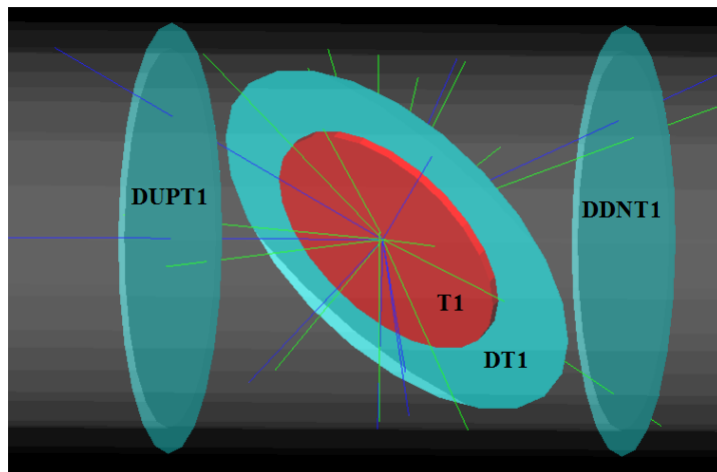


Figure 3.1: T1 is the positron production target. DUPT1 is a virtual detector located upstream of T1 to detect the incoming electron beam. DDNT1 is a virtual detector downstream of T1. DT1 is a virtual detector that is placed right after T1 parallel to it.

### 3.1.1 The Positron Beam on DDNT1

In the first step,  $1.38 \times 10^{10}$  electrons were generated with the energy distribution shown by the dotted dashed line in Figure 3.2, transported to T1, and created the positrons rep-



represented by solid the line. The dashed line is the electron energy distribution observed by DDNT1. Instead, the simulation result of  $1.38 \times 10^7$  electrons incident on T1 is drawn in Figure 3.2. The incident electrons were detected by the virtual detector DUPT1 and downstream positrons and electrons were detected by DDNT1.

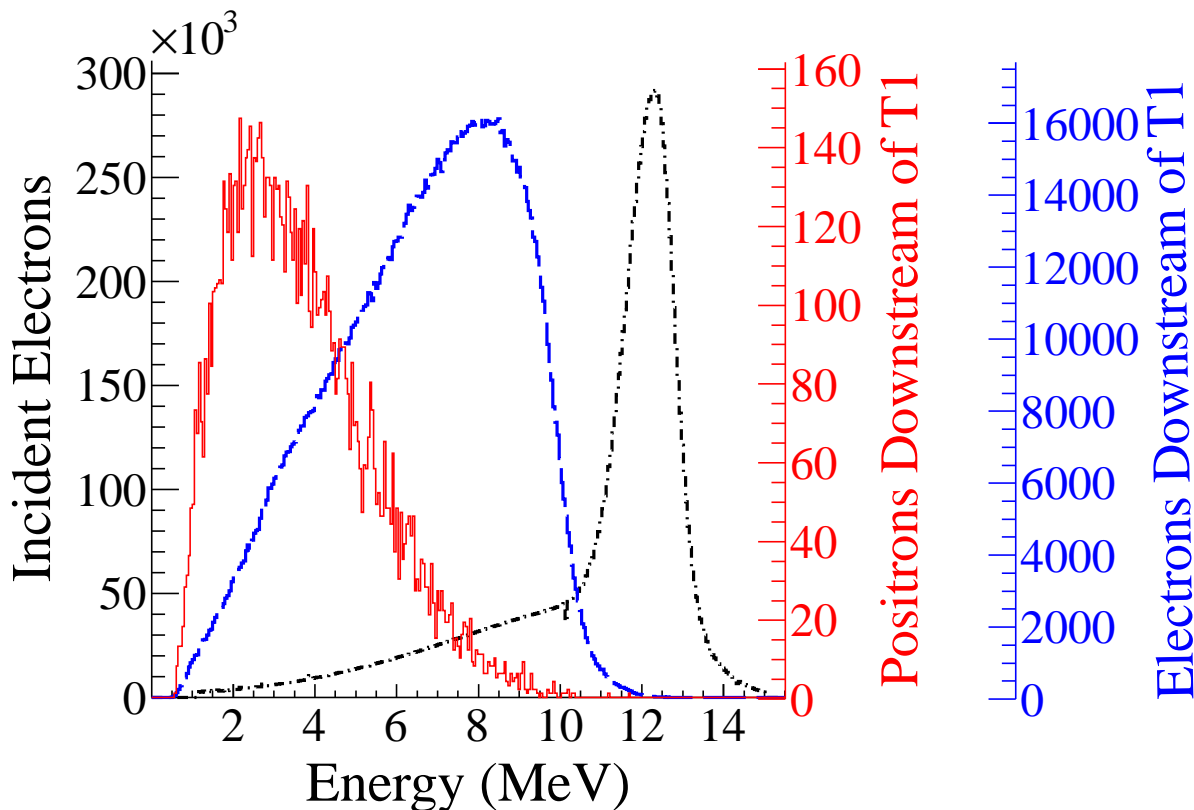
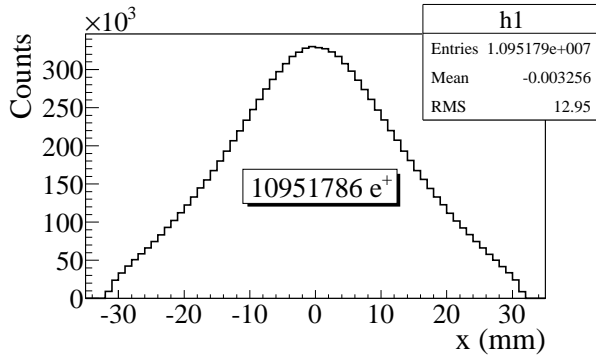
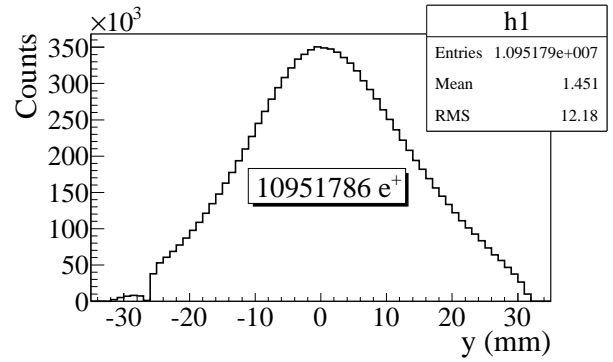


Figure 3.2: Energy distribution of incident electrons (dotted dashed line), electrons after T1 (dashed line) and created positrons (solid line). The incident electron distribution counts were weighted by 0.001.

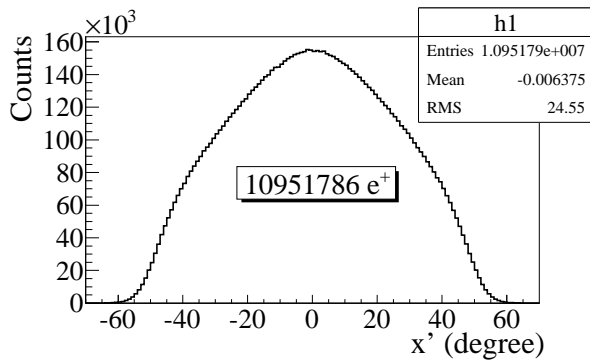
The positron spatial distribution detected by DDNT1 is shown in Figure 3.3. The  $y$  vs.  $x$  spatial distribution of the beam is shown in Figure 3.3 (e) and Figure 3.3 (f). As can be seen from Figure 3.3 (b) and (d), the  $y$  spatial distribution and divergence, defined in equation 1.4, of the positron beam have a sharp drop in counts in the region between  $-25.8$  mm and  $-27.2$  mm from the beam center. Figure 3.4 shows the geometry and location of T1 and DDNT1. If the size of T1 were to be increased, it would eventually intersect with



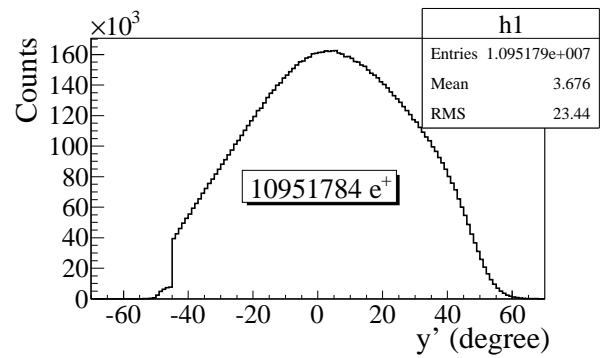
(a)  $x$  projection.



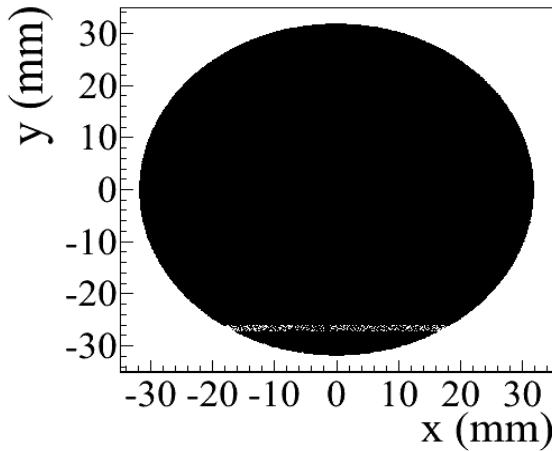
(b)  $y$  projection.



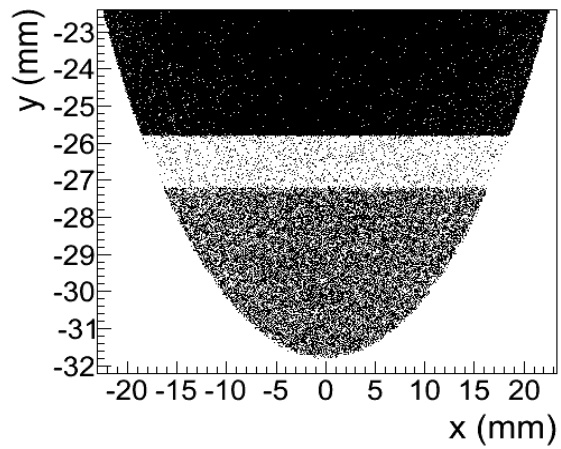
(c)  $x$  projection of the divergence.



(d)  $y$  projection of the divergence.



(e) The transverse beam profile.



(f) The transverse beam profile zoomed in.

Figure 3.3: The transverse beam projections and angular distributions of positrons detected.

DDNT1 at a distance between 25.8 mm and 27.2 mm from the beam center, *i.e.* the edge of the T1 is facing this 1.4 mm wide low count area.

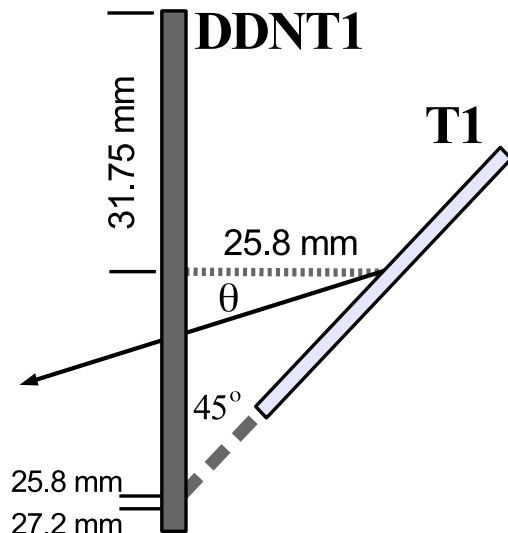


Figure 3.4: The geometry of the target T1 and the virtual detector DDNT1.

As shown in Figure 3.5, the  $y$  distribution count decreases at  $\theta = 45^\circ$ . Positrons were emitted from both the downstream and upstream side of T1. Positrons from the downstream side of T1 intersected the detector at angles below  $45^\circ$  while positrons from the upstream side of T1 begin to hit the detector at angles beyond  $45^\circ$ . Neither positrons upstream nor downstream of T1 traveled to the 1.4 mm wide low count area. Only positrons created on the edge of T1 reached the low count area between  $25.8 \text{ mm} < x < 27.2 \text{ mm}$ . As a result, the counts in this area are comparatively lower.

### 3.1.2 The Positron Beam on Virtual Detectors DQ4 and DD1

The positron beam energy distribution on virtual detectors DQ4 (Detector placed at the entrance of Q4) and DD1UP (Detector placed at the UPstream entrance of D1) are shown in Figure 3.6. Nearly 90% of the positrons are lost when transported from DQ4 to DD1UP

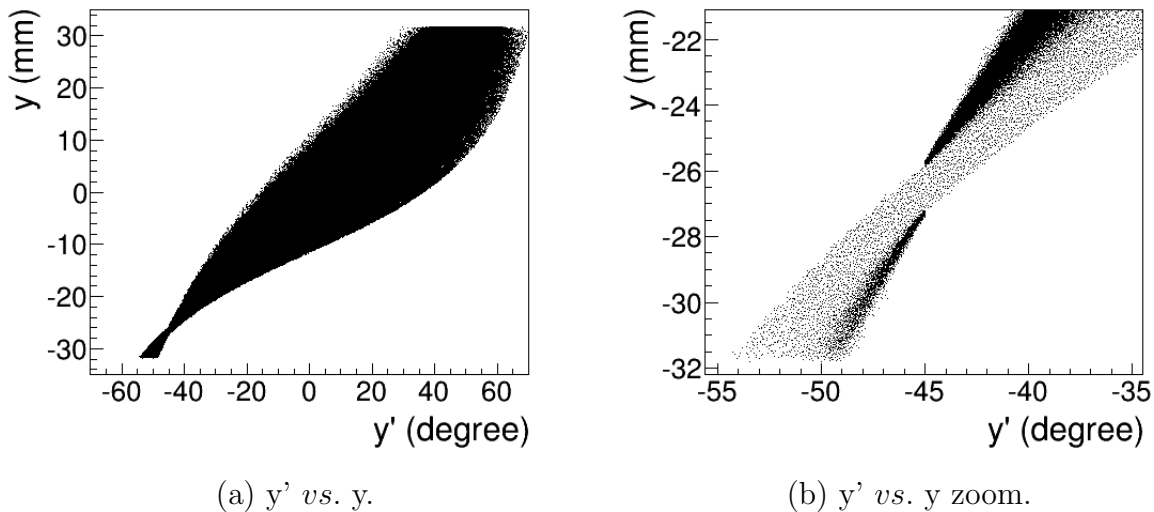
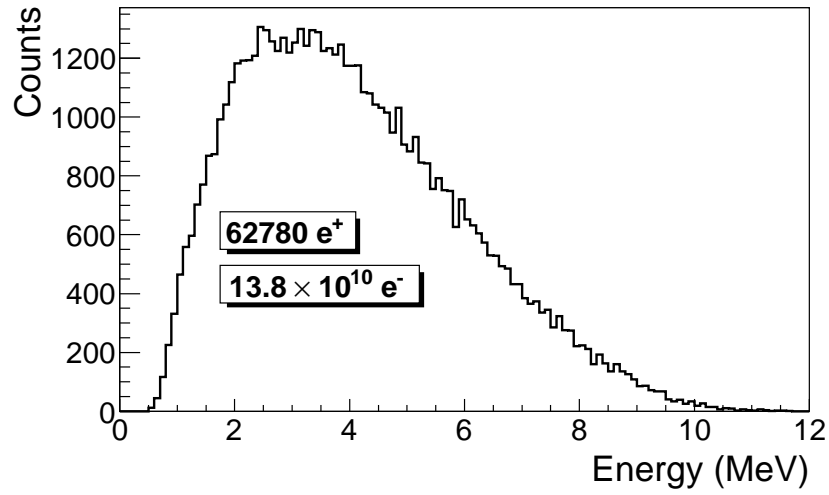


Figure 3.5: The positron beam  $y'$  vs.  $y$  detected by DDNT1.

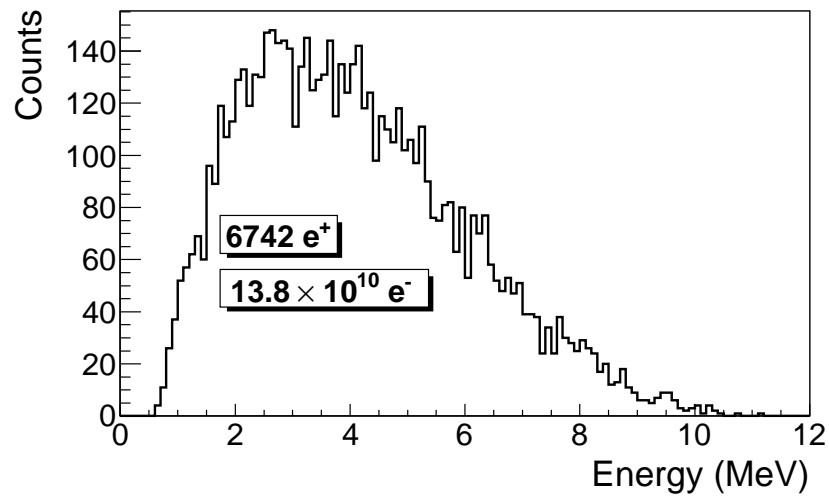
due to the large positron divergence.

## 3.2 Step 2 - The Transportation of The Positron Beam from DDNT1 to The Entrance of The First Dipole

The beam observed on detector DDNT1 in step 1 was used to generate positrons for the second step. At detector DDNT1, the higher energy positrons tend to have smaller polar angles and are closer to the beam center. Positrons were generated in 1 keV/c momentum bins with different weights, spatial, and angular distributions. The positrons are generated at DDNT1 (where they were sampled) and transported to the entrance of D1 through a quadrupole triplet as shown in Figure 3.7. The virtual detectors were placed at the entrance of Q4 (DQ4) and D1 (DD1UP) to track the positrons. The beam observed at DD1UP would be used to generate positrons in the third step.



(a) The positron energy distribution on DQ4.



(b) The positron energy distribution on DD1.

Figure 3.6: The positron beam energy distribution detected downstream of T1.

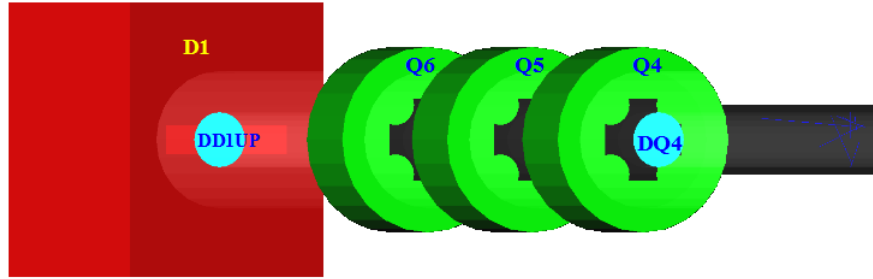


Figure 3.7: The generation and transportation of the positron beam in step 2. The virtual detectors were used to track the positrons.

### 3.3 Step 3 - The Transportation of Positrons from the Entrance of The First Dipole to T2 and The Detection of 511 keV Photons

In this step, the positron beam was generated at the entrance of the first dipole (DD1UP). The beam was bent 90° by two dipoles and transported to the annihilation target T2 located at the end of the beamline as shown in Figure 3.8.

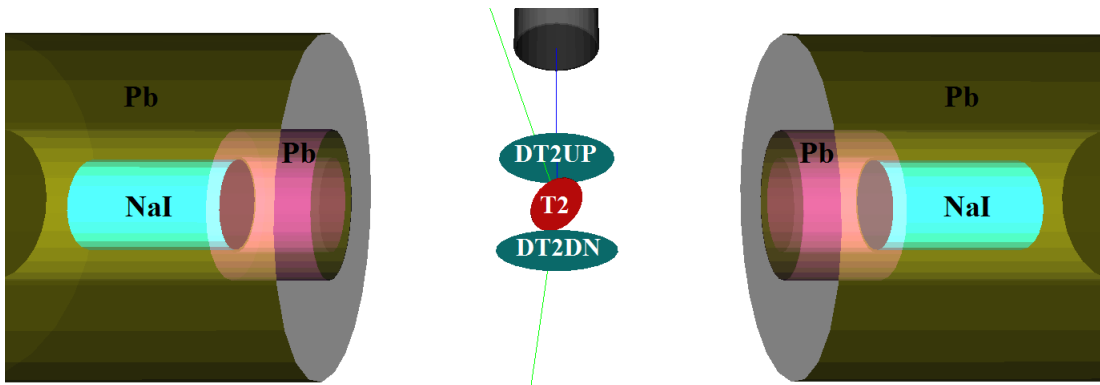


Figure 3.8: T2 and virtual detectors located upstream (DT2UP) and downstream (DT2DN) of T2 are shown at the center of the figure. NaI detectors and Pb shielding are located horizontally at two sides.

As shown in Figure 3.8, two virtual circular detectors DT2UP and DT2DN with a 48 mm diameter (48 mm is the inner diameter of the beam pipe) were placed upstream and downstream of T2 to detect positrons. Two other detectors, DT2L and DT2R with the same di-

ameters as T2 were placed on the beam left and right side parallel to T2 to detect positrons. Two virtual detectors were placed horizontally at the locations of NaI detectors, which were 170 mm away from the beamline center, to detect photons. Two inch thick Pb bricks with 2-inch diameter circular openings were positioned between T2 and the virtual detectors. Each detector was surrounded by 2'' of Pb. When a positron annihilates inside T2, two back-to-back scattered 511 keV photons are generated. An event is registered in the simulation when both NaI detectors observe a 511 keV photon.

### 3.3.1 Positrons Detected by The Detection System

The detector efficiency chart shown in Figure 3.9, obtained from Saint-Gobain Crystals [20], indicates the NaI crystal has an efficiency of 68% for 511 keV photons. If two detectors are operated in coincidence mode, the detection efficiency of the system is  $68\% \times 68\% = 46.24\%$ . Figure 3.10 shows the number of 511 keV photon pairs detected in coincidence mode (multiplied by 46.24%) and overlaid with the positrons that are detected on DDNT1.

### 3.3.2 Beam Loss Study

The positron distribution observed after T1 was used to send a sample of positrons towards the dipole D1 that would be used to create a positron event generator at the entrance to dipole D1. This procedure was repeated at D1 in order to generate a large positron sample at the annihilation target (T2). This three step procedure reduced the simulation time to generate large positron samples.  $7.253 \times 10^{16}$  electrons incident on the T1 created  $5.756 \times 10^{13}$  positrons as shown in Column 2 of Table 3.1. Columns 2 and 3 in Table 3.1 represent the number of positrons that would need to be generated in order to observe the number of positrons in the remaining columns. The number of 511 keV photon pairs detected by NaI detectors in coincidence mode are shown in the last column of Table 3.1. The number of positrons observed by virtual detectors placed along the beamline and 511 keV photon pairs

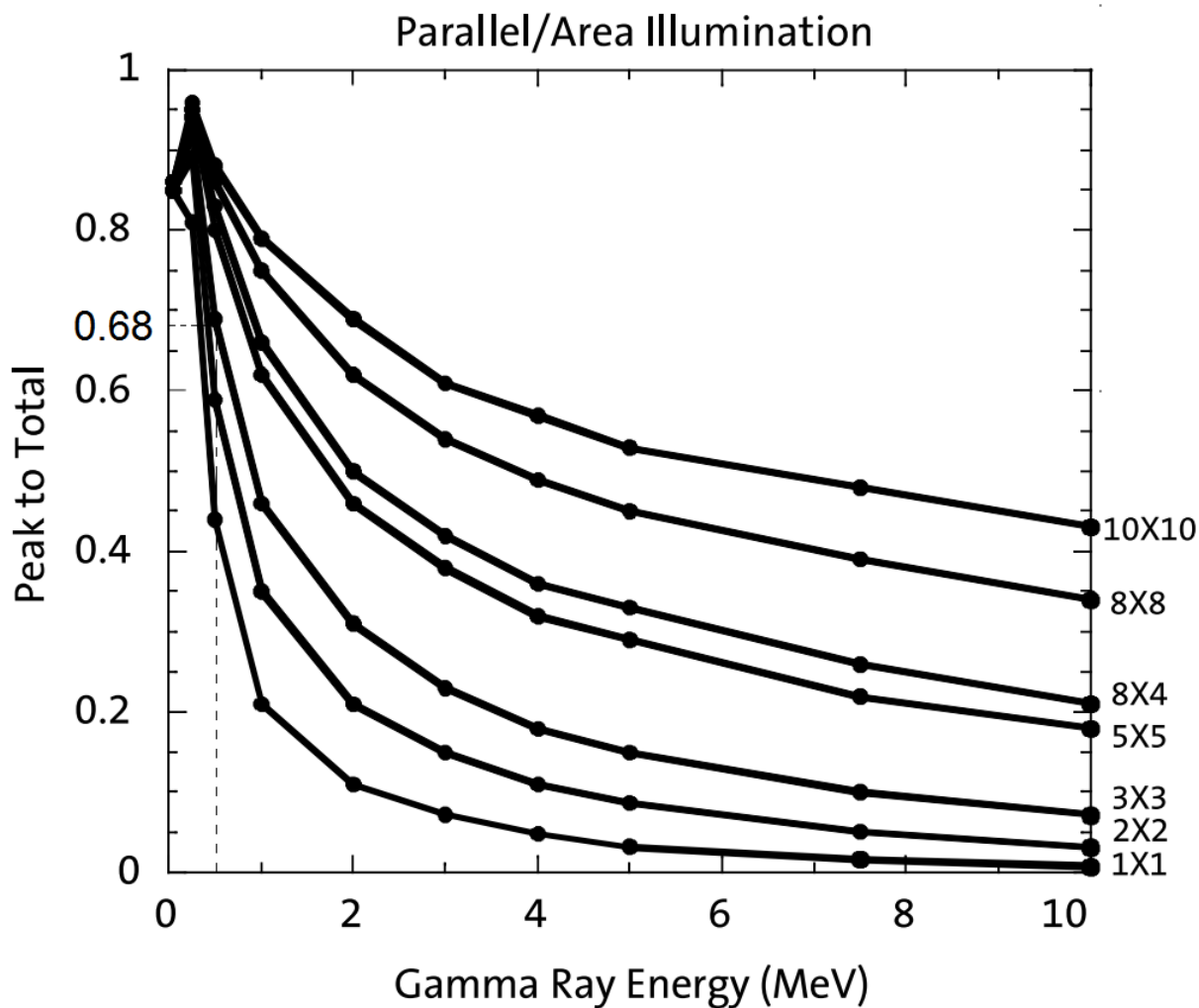


Figure 3.9: NaI detector efficiency obtained from Saint-Gobain Crystals [20]. The lines correspond to the different crystal sizes (in inches) shown on the right side of the figure.



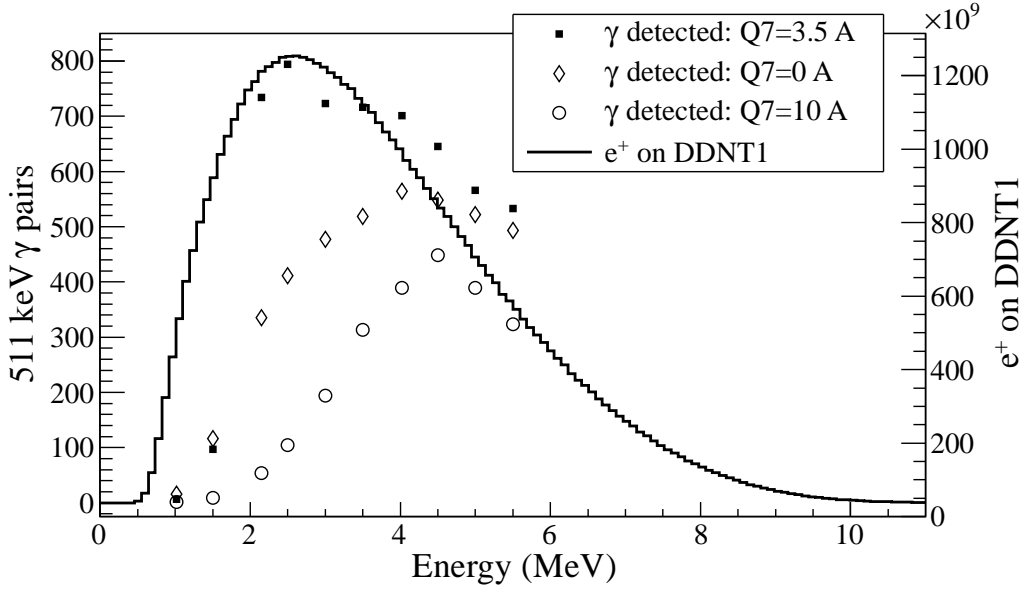


Figure 3.10: Positrons detected on virtual detector DDNT1 and 511 keV photon pairs detected by the NaI detectors in coincidence mode when Q7 is at 0 A, 3.5 A and 10 A.

detected are shown in Figure 3.11.

As shown in Table 3.1, the positron energy distribution is divided into 10 bins. At detector DDNT1 (25.8 mm after T1), there are about  $10^{12}$  positrons in each bin. At the entrance of Q4, the number of positrons dropped two orders of magnitude. This may be attributed to the solid angle that the entrance of Q4 makes with respect to T1, if one assumes T1 is a point source of positrons. The distance between T1 and the virtual detector DQ4 is 560 mm and the radius of DQ4 is 24 mm. The solid angle of the DQ4 is  $\Omega_{Q4} = \frac{\pi r^2}{d^2} = \frac{\pi 24^2}{560^2}$  rad. Positrons make up a cone with a  $45^\circ$  half angle, which is  $\Omega_{\text{beam}} = 0.6\pi$  rad in solid angle. The ratio of the two solid angles,  $\Omega_{Q4}/\Omega_{\text{beam}}$ , is 1:160, *i.e.* 1 out of 160 positrons make it from T1 to DQ4, assuming that the positron beam is isotropic inside the cone. However, the positron beam peaks at a smaller angle as shown in Figure 3.3 (c) and (d) and as a result more positrons are transported from DDNT1 to DQ4, resulting in a ratio closer to 1:100.

In a simulation where the dipoles were set to transport 3 MeV positrons, the beam energy distribution at the exit of D1, entrance of Q7, exit of Q7, entrance of D2, exit of D2, and T2

Table 3.1: Predicted Number of Positrons Transported and The Number of 511 keV Photons Detected.

Energy (MeV)	On		Enter		Exit		Enter		Exit		Reach		$\gamma$ on NaI
	DDNT1	DDNT1	Q4	D1	Enter	D1	Exit	Q7	Enter	D2	Exit	T2	
1.02 $\pm$ 0.25	$2.5 \times 10^{12}$	$2.5 \times 10^{12}$	$1.4 \times 10^{10}$	$1.4 \times 10^9$	$1.2 \times 10^8$	$1.2 \times 10^8$	$2.6 \times 10^7$	$2.7 \times 10^7$	$2.7 \times 10^6$	$1.2 \times 10^6$	$1.2 \times 10^6$	$4.3 \times 10^3$	7
1.50 $\pm$ 0.25	$4.9 \times 10^{12}$	$4.9 \times 10^{12}$	$2.8 \times 10^{10}$	$2.8 \times 10^9$	$1.8 \times 10^8$	$1.8 \times 10^8$	$9.1 \times 10^7$	$2.7 \times 10^7$	$2.7 \times 10^7$	$1.2 \times 10^7$	$1.2 \times 10^7$	$5.1 \times 10^4$	97
2.15 $\pm$ 0.25	$6.5 \times 10^{12}$	$6.5 \times 10^{12}$	$3.8 \times 10^{10}$	$3.8 \times 10^9$	$3.8 \times 10^8$	$3.8 \times 10^8$	$1.7 \times 10^8$	$7.8 \times 10^7$	$7.8 \times 10^7$	$3.6 \times 10^7$	$3.6 \times 10^7$	$4.4 \times 10^5$	734
2.50 $\pm$ 0.25	$6.8 \times 10^{12}$	$6.8 \times 10^{12}$	$4.1 \times 10^{10}$	$4.1 \times 10^9$	$4.4 \times 10^8$	$4.4 \times 10^8$	$2.3 \times 10^8$	$1.1 \times 10^8$	$1.1 \times 10^8$	$5.0 \times 10^7$	$5.0 \times 10^7$	$4.6 \times 10^5$	794
3.00 $\pm$ 0.25	$6.6 \times 10^{12}$	$6.6 \times 10^{12}$	$4.1 \times 10^{10}$	$4.1 \times 10^9$	$4.6 \times 10^8$	$4.6 \times 10^8$	$2.7 \times 10^8$	$1.3 \times 10^8$	$1.3 \times 10^8$	$6.1 \times 10^7$	$6.1 \times 10^7$	$4.5 \times 10^5$	723
3.50 $\pm$ 0.25	$6.1 \times 10^{12}$	$6.1 \times 10^{12}$	$3.9 \times 10^{10}$	$3.9 \times 10^9$	$4.4 \times 10^8$	$4.4 \times 10^8$	$2.8 \times 10^8$	$1.4 \times 10^8$	$1.4 \times 10^8$	$6.7 \times 10^7$	$6.7 \times 10^7$	$4.4 \times 10^5$	716
4.02 $\pm$ 0.25	$5.3 \times 10^{12}$	$5.3 \times 10^{12}$	$3.5 \times 10^{10}$	$3.5 \times 10^9$	$4.1 \times 10^8$	$4.1 \times 10^8$	$2.7 \times 10^8$	$1.4 \times 10^8$	$1.4 \times 10^8$	$6.9 \times 10^7$	$6.9 \times 10^7$	$4.3 \times 10^5$	702
4.50 $\pm$ 0.25	$4.6 \times 10^{12}$	$4.6 \times 10^{12}$	$3.1 \times 10^{10}$	$3.1 \times 10^9$	$3.6 \times 10^8$	$3.6 \times 10^8$	$2.5 \times 10^8$	$1.3 \times 10^8$	$1.3 \times 10^8$	$6.7 \times 10^7$	$6.7 \times 10^7$	$4.0 \times 10^5$	646
5.00 $\pm$ 0.25	$3.8 \times 10^{12}$	$3.8 \times 10^{12}$	$2.7 \times 10^{10}$	$2.7 \times 10^9$	$3.1 \times 10^8$	$3.1 \times 10^8$	$2.2 \times 10^8$	$1.2 \times 10^8$	$1.2 \times 10^8$	$6.2 \times 10^7$	$6.2 \times 10^7$	$3.6 \times 10^5$	566
5.50 $\pm$ 0.25	$3.0 \times 10^{12}$	$3.0 \times 10^{12}$	$2.2 \times 10^{10}$	$2.2 \times 10^9$	$2.6 \times 10^8$	$2.6 \times 10^8$	$1.9 \times 10^8$	$1.0 \times 10^8$	$1.0 \times 10^8$	$5.6 \times 10^7$	$5.6 \times 10^7$	$3.3 \times 10^5$	533

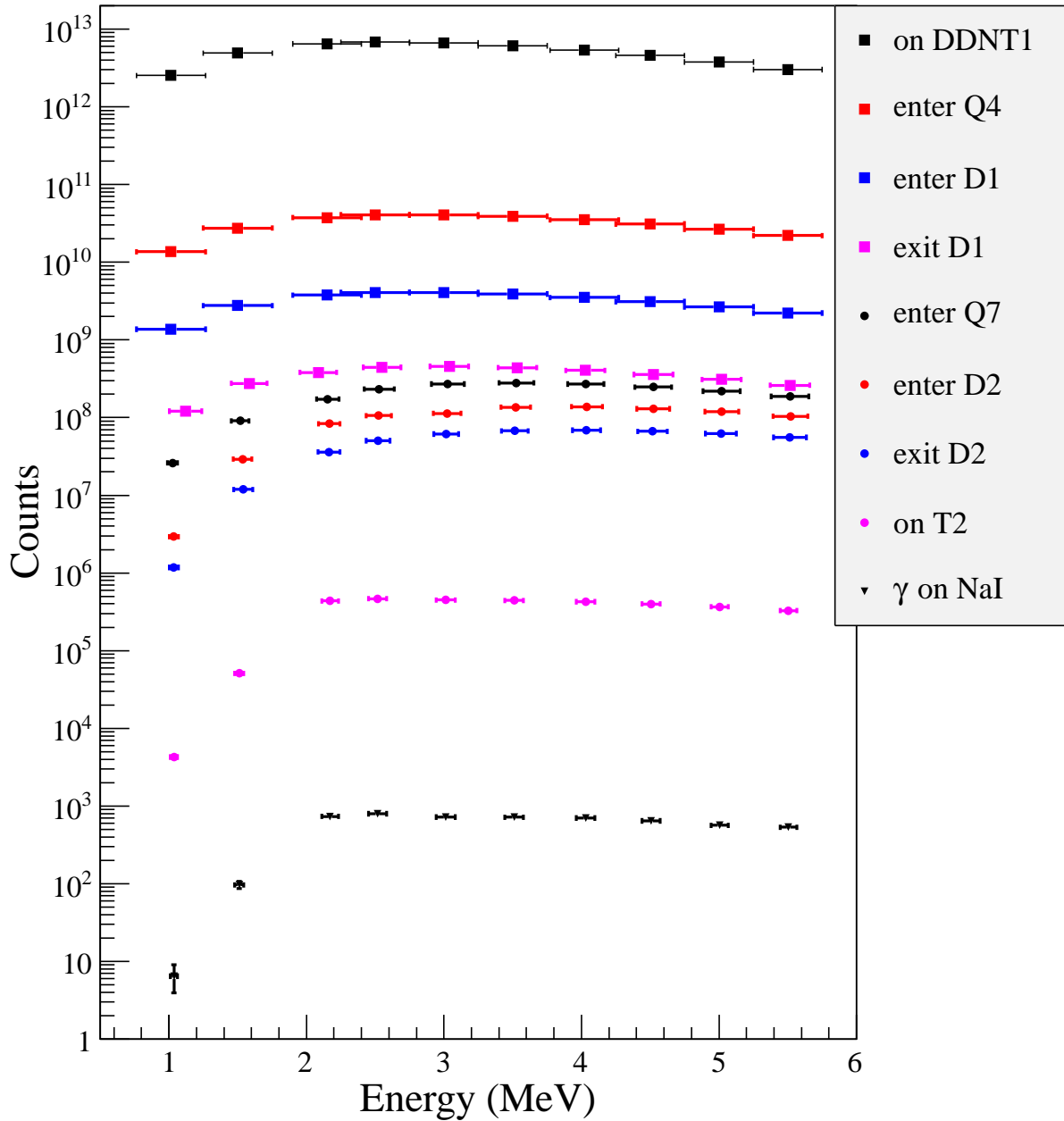


Figure 3.11: Predicted number of positrons transported. Black cube: positrons incident on DDNT1. Red cube: positrons entered Q4. Blue cube: positrons entered D1. Magenta cube: positrons exited D1. Black circle: positrons entered Q7. Red circle: positrons entered D2. Blue circle: positrons exited D2. Magenta circle: positrons incident on DT2UP. Black triangle: 511 keV photons detected by NaI detectors in coincidence mode.

Table 3.2: The Positron Beam Loss Along The Beamline.

Beam Sample Locations	Absolute Counts	Relative Counts
e <sup>+</sup> on DDNT1	$6.6 \times 10^{12}$	$9.4 \times 10^{10}$
e <sup>+</sup> enter Q4	$4.1 \times 10^{10}$	$5.8 \times 10^7$
e <sup>+</sup> enter D1	$4.1 \times 10^9$	$5.8 \times 10^6$
e <sup>+</sup> exit D1	$4.6 \times 10^8$	$6.6 \times 10^5$
e <sup>+</sup> enter Q7	$2.7 \times 10^8$	$3.8 \times 10^5$
e <sup>+</sup> enter D2	$1.3 \times 10^8$	$1.9 \times 10^5$
e <sup>+</sup> exit D2	$6.1 \times 10^7$	$8.7 \times 10^4$
e <sup>+</sup> on T2	$4.4 \times 10^5$	$6.3 \times 10^2$
e <sup>+</sup> annihilated in T2	$2.5 \times 10^5$	$3.6 \times 10^2$
511 keV photons on NaI	723	1

are shown in Figure 3.12 and Table 3.2. In Table 3.2, the relative counts reported in the last column are obtained by dividing the second column by 723, the number of 511 keV photons detected by NaI detectors in coincidence mode.

The dipoles in the simulation were set to transport 3 MeV positrons to the annihilation target T2, where 58% of the positrons annihilated and created 511 keV photon pairs. 0.7% of the photon pairs are lost when passing through the vacuum windows. The left NaI detector observed 2897 511 keV photons and the right one detected 4100. The ratio of 511 keV photon pairs created in T2 to those that made it to the right and the left NaI are 88:1 and 62:1 respectively. This is comparable to the solid angle made by out going photons to the solid angle made by a NaI detector.

The distance between the NaI detectors and the beamline center is 170 cm. The Pb shielding has a hole facing T2 with a 2 inch diameter. Assuming positrons annihilated at the center of T2, the solid angle made by a NaI detector is  $\Omega = \frac{\pi r^2}{d^2} = \frac{\pi 25.4^2}{170^2}$  rad. The 511 keV photons created during the annihilation make a solid angle of  $2\pi$  rad considering each side of T2 is facing one detector. The ratio of  $2\pi$  rad to solid angle of T2 is about 90:1.

1518 511 keV photon pairs are detected by NaI detectors in coincidence mode. The ratio of 511 keV photon pairs created to the ones detected in coincidence mode is 168:1. Counting

photons in coincidence mode with the 46.24% detection efficiency of the system cut the rate in half.

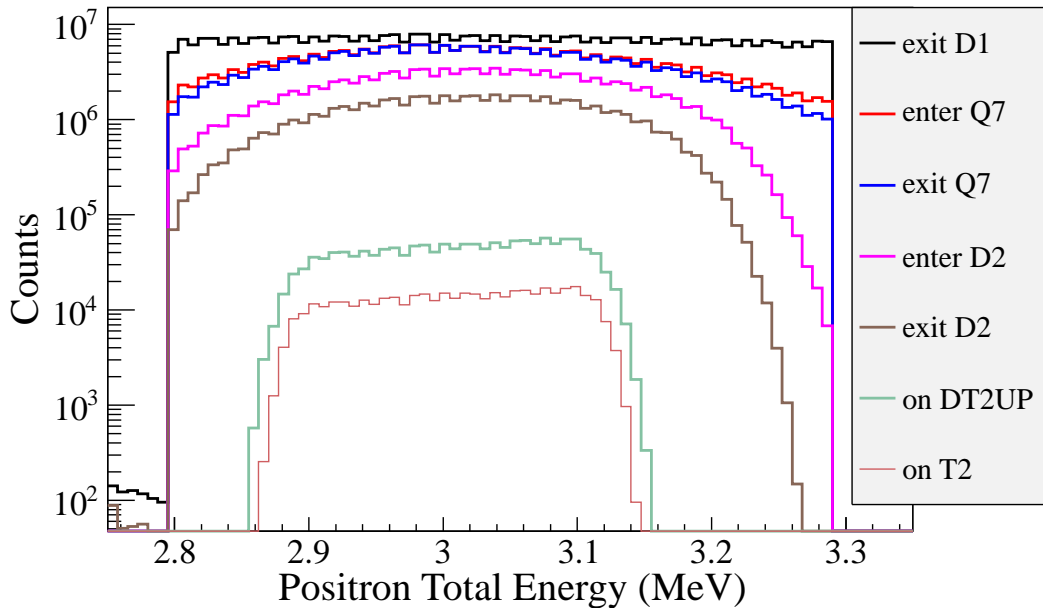


Figure 3.12: Positrons transported when dipoles are set to bend 3 MeV positrons.

### 3.3.3 Analysis of the Photon Count Asymmetry in NaI Detectors

In the simulation of section 3.3.2, the right NaI detector observed more 511 keV photons than the left. Eight virtual NaI detectors were placed as shown in Figure 3.13 to study this count asymmetry. The orientation of T2 with respect to the incident positron beam was simulated for three cases. In the first case, the photon count rate was predicted by the simulation when the face norm of T2 is parallel to the beam. In the second case, T2 was rotated clockwise (starting with the T2 location in the first case) about the x-axis (axis points beam left) by  $45^\circ$  leaving the upstream side of T2 facing downward as shown in Figure 3.13 (a). In the third case, T2 was rotated clockwise about the y-axis (axis points beam up) by  $45^\circ$  such that it is facing the beam right NaI detector as shown in Figure 3.13 (b). The setup in the third case is similar to the setup in the experiment and the simulation in section 3.3.2. The 511 keV photon counts observed by eight virtual NaI detectors for one million positrons

Table 3.3: Number of 511 keV photons observed by the NaI detectors.

T2 Placement	Exp.	Perp. to Beam	Face Down	Face Down	Face Down	Face Down
Energy	3 MeV	3 MeV	3 MeV	1 MeV	6 MeV	10 MeV
NaI Right	18085	7610	7160	10315	6209	4436
NaI Left	12798	7651	7114	10254	6111	4487
NaI Top Right	7050	7580	12964	12371	14698	10636
NaI Bottom Left	7084	7609	18563	20238	15989	10239
NaI Top	12687	7599	14810	14332	16131	11479
NaI Bottom	18008	7609	18874	20193	16950	11181
NaI Top Left	14632	7656	12818	12268	14812	10735
NaI Bottom Right	18764	7623	18415	20197	16004	10317

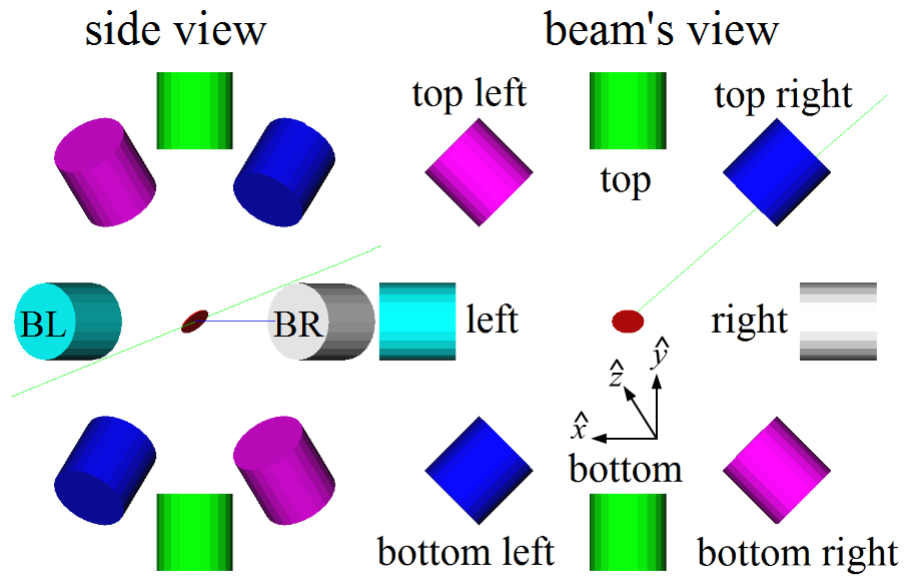
are given in Table 3.3 for each configuration.

When T2 was placed perpendicular to the incoming positron beam, the 511 keV photons created inside T2 have the same probability to escape from T2 and reach any one of the detectors. As shown in the third column of Table 3.3, all eight detectors observed a similar number of photons.

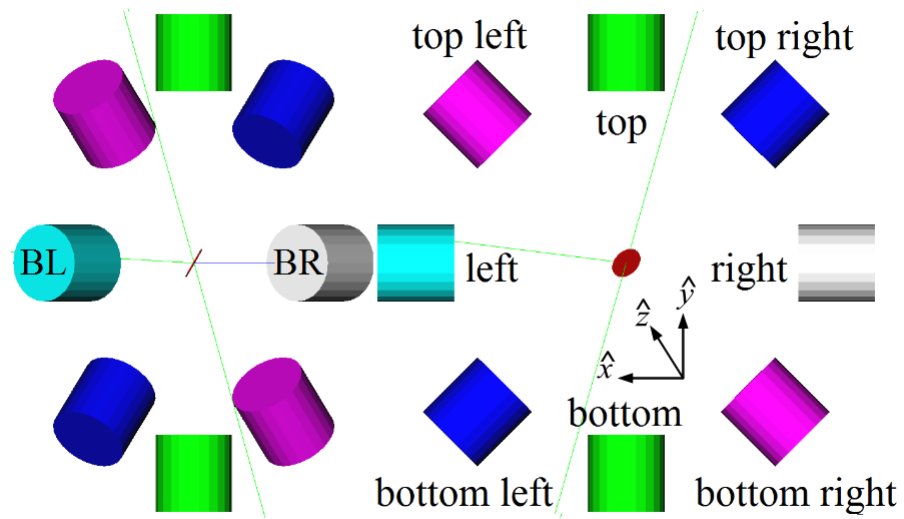
In a separate simulation, T2 was positioned as in the first case and impinged by 1, 3, 6, 10 MeV positrons. The average distance traveled by positrons inside T2 before annihilation was  $0.0847 \pm 0.0001$ ,  $0.3006 \pm 0.0004$ ,  $0.511 \pm 0.001$ ,  $0.564 \pm 0.008$  mm for the four energies respectively. In another GEANT4 simulation, T2 was positioned according to the second case and two virtual NaI detectors were placed on the top and the bottom of T2. The bottom detector observed more photons than the top when 511 keV photons were generated 0.3006 mm inside T2 isotropically. Photons are more likely to reach the bottom detector because they would travel through a thinner layer of tungsten to reach the bottom detector.

In the second case, shown in Figure 3.13 (a), the left and the right NaI detectors had the lowest counts for 3 MeV positrons as shown in the fourth column of Table 3.3. There is a smaller detection probability for a photon traversing T2 in the radial direction towards the left/right detectors than the top/bottom surfaces of T2 due to the amount of material.

The average distance traveled by 3 MeV positrons inside T2 before annihilation was



(a)



(b)

Figure 3.13: NaI detector locations around T2. The positron beam (blue line) is traveling along the  $z$ -axis (into the paper). (a) T2 was rotated clockwise about the  $x$ -axis by  $45^\circ$  positioning the upstream side of the T2 such that it faces the bottom NaI detector. (b) T2 was positioned as in the experiment. It was first rotated to the position as in (a), then it was rotated clockwise about the  $y$ -axis by  $45^\circ$ , positioning the upstream side of the T2 such that it faces the beam right NaI detector.

$0.3006 \pm 0.0004$  mm. In this case, positrons annihilated near the upstream face of T2. For this reason, the bottom, bottom right, and bottom left NaI detectors (facing the upstream side of T2) observed more photons than the top, top right, and top left as shown in the fourth column of Table 3.3.

The lower the positron beam energy, the smaller the annihilation depth, and the bigger asymmetry in the counts. As shown in the fourth and fifth columns of Table 3.3, more/less 511 keV photons were observed on the bottom/top detectors with the 1 MeV positron beam than with the 3 MeV. As the positron beam energy increases, as shown in the sixth and seventh columns of Table 3.3, the top and bottom detectors observed a similar number of photons, because positrons annihilate more uniformly inside T2 and the asymmetry in the counts decreases. With the increasing positron beam energy, fewer positrons were annihilated inside T2 and more penetrated through, as shown in the top two rows of Table 3.3.

For the third case, shown in Figure 3.13 (b), the top right and left bottom detectors observed the lowest counts, because a photon would need to travel in the radial direction to reach these two detectors as shown in the second column of Table 3.3. The right, bottom and bottom right (facing upstream face of T2) observed more photons than the left, top, top left.

According to the simulation, the asymmetry in the photon counts was due the average positron annihilation depth and the photon attenuation inside T2. Low energy positrons tend to annihilate and produce photon pairs near the incident surface. The created photons are more likely to be detected from the incident surface. In the experiment and the simulation, the right NaI detector was facing the upstream side of T2 and observed more 511 keV photons than the left.

### **3.4 Quadrupole Triplet Collection Efficiency Study**

In this simulation, 5,475,869,400 positrons were generated at DDNT1 and transported to DD1 to study the quadrupole triplet positron collection and transportation efficiency. Six



quadrupole current settings of the triplet system were simulated as shown in Table 3.4. For different quadrupole current settings, no significant differences were observed in the number of positrons, transverse beam profiles and momentum distributions. The ratio of positrons generated at DDNT1 to the ones that enter D1 is 1525:1.

### 3.5 Systematic Errors

Systematic errors for the positron counts were estimated by carrying out simulations with different magnet settings as shown in Table 3.5. The magnet settings are indicated in the top three rows of Table 3.5. The transported positron energy is given in the first column. The 511 keV photon pairs counted in coincidence mode (*i.e.* the original count multiplied by 46.42%) for different magnet settings are given in the corresponding columns below.

The uncertainty of the magnet power supply is 0.1 A. The “Max”/“Min” in the table refers to the Maximum/Minimum magnetic field strength when the magnet coil current is at  $I_{\max}/I_{\min}$ , where  $I_{\max} = I_{\text{def}} + 0.1$  A and  $I_{\min} = I_{\text{def}} - 0.1$  A. “def” refers to the default magnetic field strength of the magnet.

The average counts and fractional errors are shown in the last two columns of Table 3.5. The fractional error in the 511 keV photon pair counts is calculated by dividing the standard deviation of counts by the counts in default magnet setting, *i.e.*  $\frac{\text{standard deviation of counts}}{\text{counts in default setting}}$ .

Table 3.4: Quadrupole Triplet System Collection and Transportation Efficiency Data.

Q4	Q5	Q6	Entries	$x$	$\sigma_x$	$y$	$\sigma_y$	$P_x$	$\sigma_{P_x}$	$P_y$	$\sigma_{P_y}$	$P_z$	$\sigma_{P_z}$
A	A	A		mm	mm	mm	mm	MeV	MeV	MeV	MeV	MeV	MeV
-1	2	-1	3587220	-0.005	12	0.030	12	$3.0 \times 10^{-5}$	0.0461	-0.00216	0.04553	3.848	1.875
-2	4	-2	3591423	-0.012	12	0.049	12	$2.2 \times 10^{-5}$	0.0461	-0.00211	0.04554	3.848	1.875
1	-2	1	3591509	-0.009	12	0.040	12	$-1.5 \times 10^{-5}$	0.0462	-0.00216	0.04557	3.849	1.876
1	2	1	3589854	-0.005	12	0.034	12	$-1.8 \times 10^{-5}$	0.0462	-0.00216	0.04556	3.849	1.876
2	-4	2	3592977	-0.007	12	0.032	12	$-3.3 \times 10^{-6}$	0.0462	-0.00217	0.04549	3.849	1.876
2	4	2	3589495	-0.004	12	0.033	12	$3.0 \times 10^{-6}$	0.0462	-0.00218	0.04554	3.849	1.875

Table 3.5: Systematic Error Study: Counts of 511 keV Photon Pairs for Different Magnet Settings.

D1	Max	Min	Max	Min	Max	Min	Max	Min	Min	Min	Def	Def	Def	Def	Average		Fractional Error
															Average	Fractional Error	
Q7	Max	Def	Max	Def	Max	Def	Max	Def	Max	Def	Max	Def	Max	Def	Max	Def	
D2	Max	Min	Def	Def	Def	Def	Def	Def	Def	Def	Def	Def	Def	Def	Average <td>Fractional Error</td> <td></td>	Fractional Error	
Energy (MeV)																	
0.765	12	2	3	1	1	3	3	0	3	4	3	4	3	4	4	4	57.3 %
1.25 - 1.75	95	75	70	86	85	92	129	86	92	90	129	86	97	90	90	90	17.6 %
1.85 - 2.35	674	724	737	769	686	747	803	681	747	728	803	681	734	728	728	728	5.8 %
2.25 - 2.75	781	755	753	759	772	963	794	763	963	793	794	763	794	793	793	793	8.3 %
2.75 - 3.25	739	737	765	752	738	698	738	757	698	739	738	757	723	739	739	739	2.7 %
3.25 - 3.75	713	699	747	712	707	751	718	705	751	719	718	705	716	719	719	719	2.5 %
3.77 - 4.27	690	708	715	676	704	658	706	715	658	697	706	715	701	697	697	697	2.7 %
4.25 - 4.75	627	666	634	646	635	675	637	653	675	646	637	653	646	646	646	646	2.5 %
4.75 - 5.25	558	595	594	603	606	688	582	582	688	597	582	582	566	597	597	597	6.7 %
5.25 - 5.75	513	536	535	522	525	535	518	544	535	529	518	544	533	529	529	529	1.9 %

# Chapter 4

## Data Analysis

### 4.1 HRRL Emittance Measurement

A quadrupole scanning method was used to measure the accelerator's emittance. The quadrupole current is changed to alter the strength and direction of the quadrupole magnetic field such that a measurable change in the beam shape is seen by the OTR system. Initially, the beam was steered by the quadrupole indicating that the beam was not entering along the quadrupole's central axis. Several magnetic elements upstream of this quadrupole were adjusted to align the incident electron beam with the quadrupole's central axis. First, the beam current observed by a Faraday cup located at the end of beam line was maximized using upstream steering coils within the linac nearest the gun. Second, the first solenoid nearest the linac gun was used to focus the electron beam on the OTR screen. Steering coils were adjusted to maximize the beam current to the Faraday cup and minimize the deflection of the beam by the quadrupole. A second solenoid and the last steering magnet shown in Figure 2.1, both near the exit of the linac, were used in the final step to optimize the beam spot size on the OTR target and maximize the Faraday cup current. A configuration was found that minimized the electron beam deflection when the quadrupole current was altered during the emittance measurements.

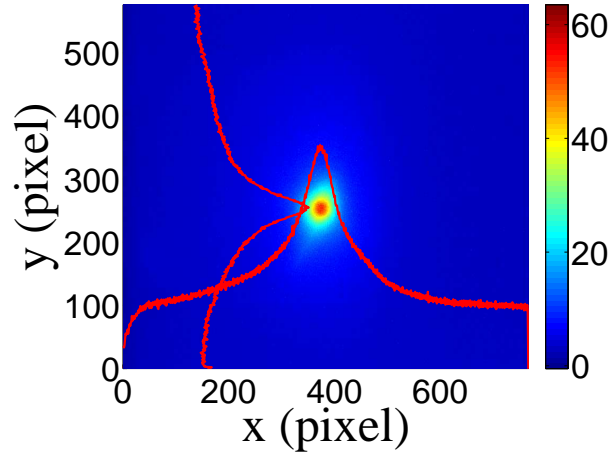
The emittance measurement was performed using an electron beam energy of 15 MeV and a 200 ns long macro pulse of 40 mA electron current. The current in the first quadrupole after the exit of the linac was changed from  $-5$  A to  $+5$  A with an increment of 0.2 A. Seven measurements were taken at each current step in order to determine the average beam width and the variance. Background measurements were taken by turning the linac's electron gun

off while keep the RF on. OTR images before and after background subtraction are shown in Figure 4.1. A small dark current is visible in Figure 4.1 (b) that is known to be generated when electrons are pulled off the cavity wall and accelerated.

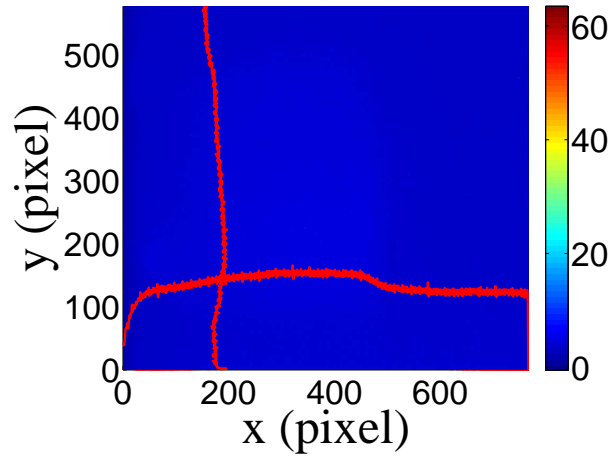
The electron beam energy was measured using a dipole magnet downstream of the quadrupole used for the emittance measurements. Prior to energizing the dipole, the electron micro-pulse bunch charge passing through the dipole was measured using a Faraday cup located approximately 50 cm downstream of the OTR screen. The dipole current was adjusted until a maximum beam current was observed on another Faraday cup located just after the 45 degree exit port of the dipole. A magnetic field map of the dipole indicates that the electron beam energy was  $15 \pm 1.6$  MeV.

Images from the JAI camera were calibrated using the OTR target frame. An LED was used to illuminate the OTR aluminum frame that has a known inner diameter of 31.75 mm. Image processing software was used to inscribe a circle on the image to measure the circular OTR inner frame in units of pixels. The scaling factor can be obtained by dividing this length with the number of pixels observed. The result is a horizontal scaling factor of  $0.04327 \pm 0.00016$  mm/pixel and vertical scaling factor of  $0.04204 \pm 0.00018$  mm/pixel. Digital images from the JAI camera were extracted in a matrix format in order to take projections on both axes and perform a Gaussian fit. The observed image profiles were not well described by a single Gaussian distribution.

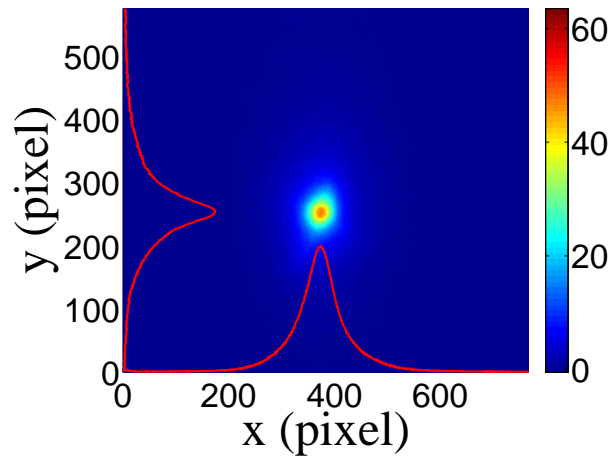
The profiles may be described using a Lorentzian distribution, however, the rms of the Lorentzian function is not defined. A super Gaussian distribution was used [22], because it has a sharper distribution than Gaussian and, unlike Lorentzian, the rms values may be directly extracted. The super Gaussian reduced the Chi-square per degree of freedom by a factor of ten compared to a typical Gaussian fit. The beam spot, beam projections, and fits are shown in Figure 4.2. In a typical Gaussian distribution,  $\phi(x) = \frac{1}{\sqrt{2\pi}}e^{-\frac{1}{2}x^2}$ , the independent variable  $x$  is raised to the 2nd power while in the super Gaussian it is raised to a power smaller than 2. For example, the beam projections shown in Figure 4.2 were fitted with the super Gaussian distributions. The variable  $x$  on the exponent was raised to 0.9053



(a)



(b)



(c)

Figure 4.1: Digital image from the OTR screen; (a) an image taken with the beam on, (b) a background image taken with the RF on but the electron gun off, (c) The background subtracted beam image ((a)-(b)).

( $x$ -projection) and 1.0427 ( $y$ -projection).

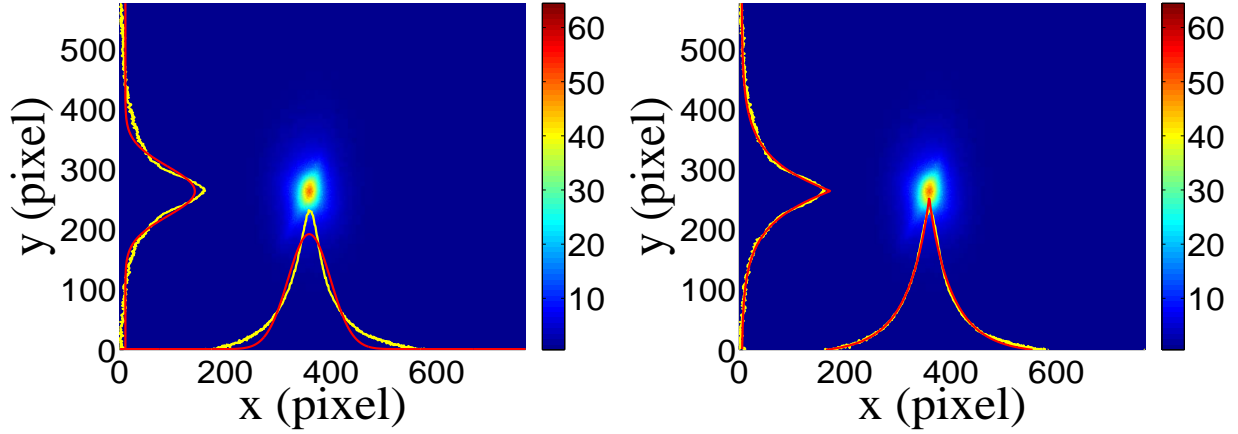


Figure 4.2: Gaussian and super Gaussian fits for beam projections. The beam images is background subtracted image and taken when quadrupole magnets are turned off. Left image is Gaussian fit and right image is super Gaussian fit.

Figure 4.3 shows the square of the rms ( $\sigma_s^2$ ) vs  $k_1 L$  for  $x$  (horizontal) and  $y$  (vertical) beam projections along with the parabolic fits using Eq. 4.3. The emittance and Twiss parameters from these fits are summarized in Table 4.1. The MATLAB [21] scripts used to calculate emittance and Twiss parameters are given in appendix B.

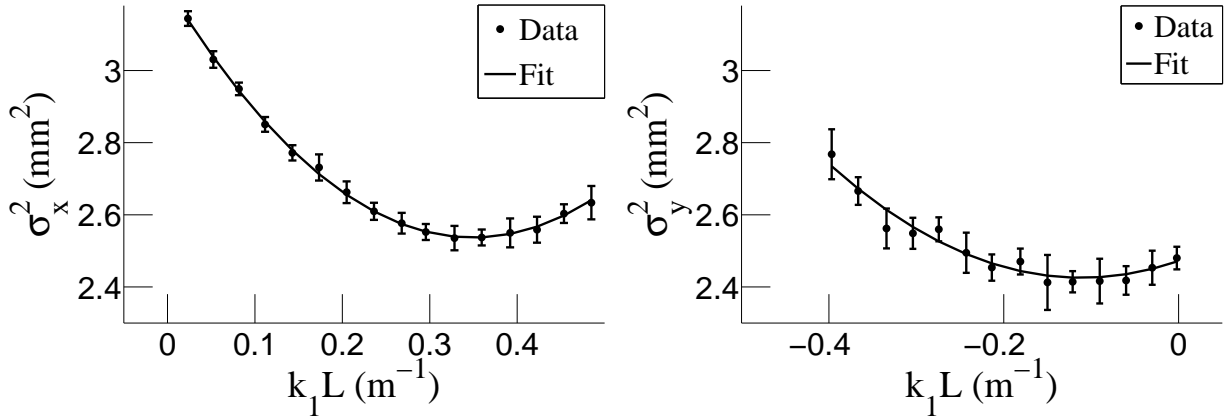


Figure 4.3: Square of rms values and parabolic fittings.

Table 4.1: Emittance Measurement Results

Parameter	Unit	Value
projected emittance $\epsilon_x$	$\mu\text{m}$	$0.37 \pm 0.02$
projected emittance $\epsilon_y$	$\mu\text{m}$	$0.30 \pm 0.04$
$\beta_x$ -function	m	$1.40 \pm 0.06$
$\beta_y$ -function	m	$1.17 \pm 0.13$
$\alpha_x$ -function	rad	$0.97 \pm 0.06$
$\alpha_y$ -function	rad	$0.24 \pm 0.07$
micro-pulse charge	pC	11
micro-pulse length	ps	35
energy of the beam $E$	MeV	$15 \pm 1.6$
relative energy spread $\Delta E/E$	%	10.4

## 4.2 Measurement of HRRL Electron Beam Energy Spread at 12 MeV

The HRRL energy profile was measured when it was tuned to accelerate electrons to 12 MeV peak energy. A Faraday cup was placed at the end of the 45 degree beamline to measure the electron beam current when D1 was on and D2 was off. The dipole coil current for D1 was changed in 1 A increments. As the dipole coil current was changed, the energy of the electrons transported to the Faraday cup would change as described in Appendix A. Figure 4.4 illustrates a measurement of the 12 MeV peak illustrating the observed low energy tail. The HRRL energy profile can be described by overlapping two skewed Gaussian fits [22]. The fit function is given by

$$G(En) = A_1 e^{\frac{-(En-\mu_1)^2}{2\{\sigma_1[1+\text{sgn}(En-\mu_1)]\}^2}} + A_2 e^{\frac{-(En-\mu_2)^2}{2\{\sigma_2[1+\text{sgn}(En-\mu_2)]\}^2}}, \quad (4.1)$$



where  $sgn$  is the sign function, that is defined as

$$sgn = \begin{cases} -1 & (x < 0) \\ 0 & (x = 0) \\ 1 & (x > 0). \end{cases}$$

The other variables are defined as  $\sigma_1 = \frac{\sigma_{r,1} + \sigma_{l,1}}{2}$ ,  $\sigma_2 = \frac{\sigma_{r,2} + \sigma_{l,2}}{2}$ ,  $E_1 = \frac{\sigma_{r,1} - \sigma_{l,1}}{\sigma_{r,1} + \sigma_{l,1}}$ , and  $E_2 = \frac{\sigma_{r,2} - \sigma_{l,2}}{\sigma_{r,2} + \sigma_{l,2}}$ . The measurement results and fits are shown in Figure 4.4 and in Table 4.2.

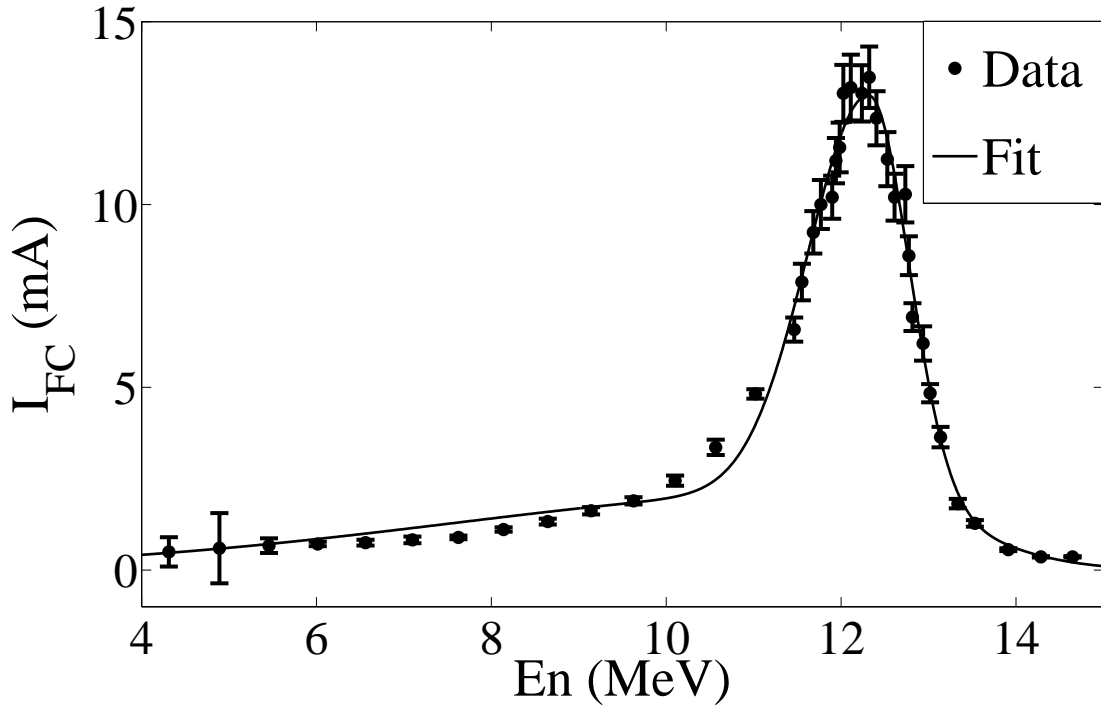


Figure 4.4: HRRL energy scan (dots) and fit (line) with two skewed Gaussian distribution.

### 4.3 The Electron Beam Current Measurement

A scintillator was placed between Q9 and Q10, as shown in Figure 4.5, to monitor the electron beam current. The electron beam current was changed incrementally to measure the correlation between the scintillator and the accelerated electron beam. The beam current was

Table 4.2: Fit Parameters for Two Skewed Gaussian.

Parameter	Notation	Unit	First Gaussian	Second Gaussian
amplitude	A	mA	2.14	10.88
mean	$\mu$	MeV	12.07	12.32
sigma left	$\sigma_L$	MeV	4.47	0.70
sigma right	$\sigma_R$	MeV	1.20	0.45

Table 4.3: Scintillator Calibration Data.

Run Number	Faraday Cup Charge Area (nVs)	Mean of ADC Channel 9
3703	$1201 \pm 10$	$1126 \pm 0.8$
3705	$777 \pm 110$	$791.8 \pm 0.6$
3706	$367.7 \pm 2.3$	$242.1 \pm 0.3$

measured using FC1 and the output was integrated using an oscilloscope. The scintillator output was integrated using an ADC (CAEN Mod. V792). As the electron beam current was decreased, the signal observed on the oscilloscope decreased and the ADC measured less charge from the scintillator as shown in Figure 4.6. A linear fit to data resulted a linear relation

$$Q_{e^-}(i) = (0.0186 \pm 0.0028)i + 2.79 \pm 0.08 \text{ C}, \quad (4.2)$$

where  $i$  is ADC channel number and  $Q$  is the accelerated electron beam charge. The fit is shown in Figure 4.7.

When running in coincidence mode, the electron beam current is sampled by the scintillator only when a coincidence event occurs causing a trigger that gates the ADC and measures the scintillator output for that positron coincidence event. The charge measured by the ADC is the total charge of the electron pulses that created the positron events. The number of beam pulses are counted using a scaler. The total charge on T1 for the entire run

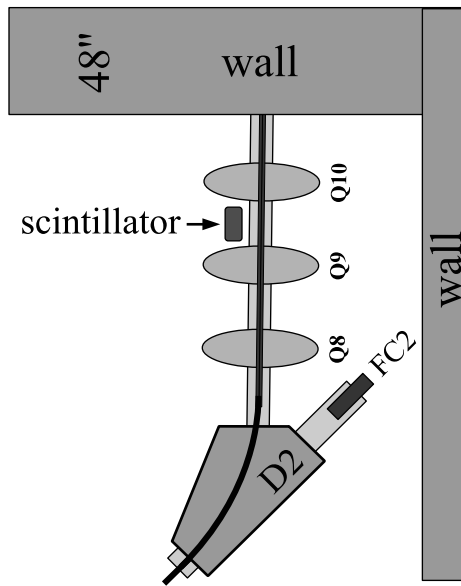


Figure 4.5: The electron beam monitor.

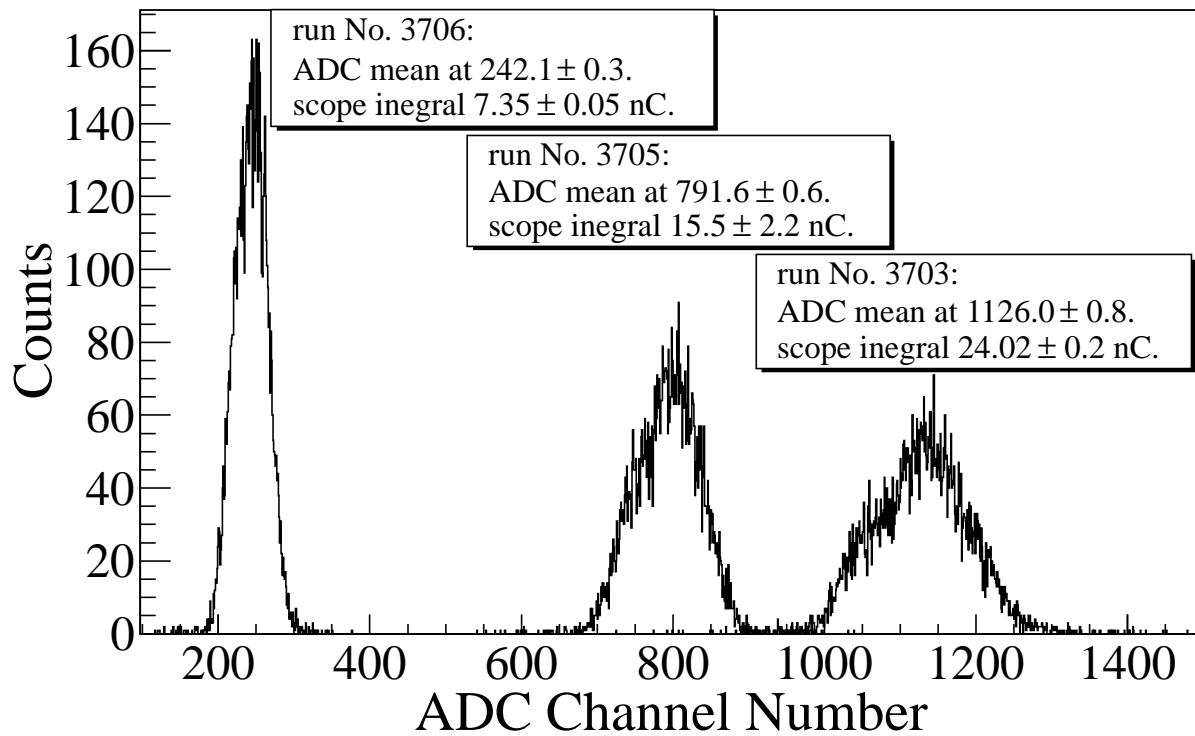


Figure 4.6: The photon flux detected using scintillator. The mean of the ADC channel decreased linearly as the electron beam current was decreased.

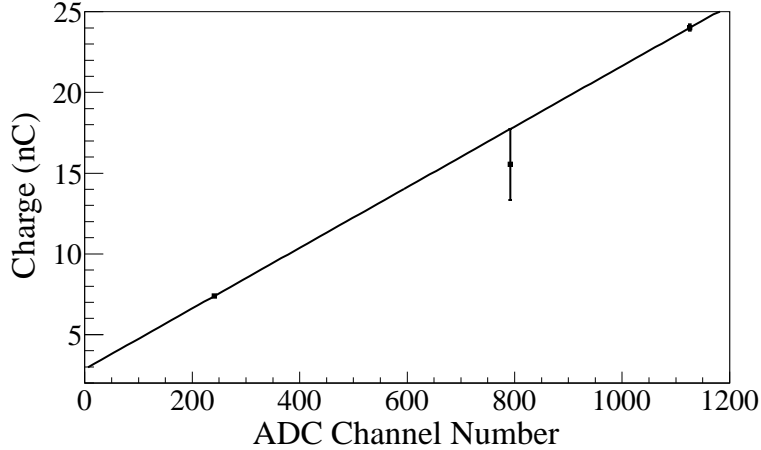


Figure 4.7: Fit for accelerator beam current *v.s.* the ADC channel.

is estimated using

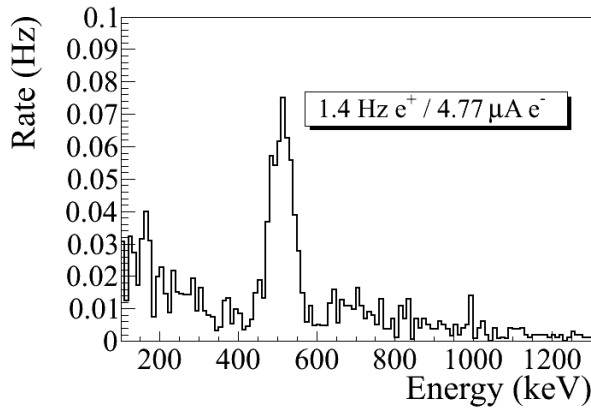
$$Q_C = \left( \sum_i^N 0.0186i \times (\text{bin content}[i]) + 2.79 \right) \times \frac{(\# \text{ of beam pulses})}{(\# \text{ of events})}. \quad (4.3)$$

## 4.4 Positron Rate Estimation in Coincidence Mode

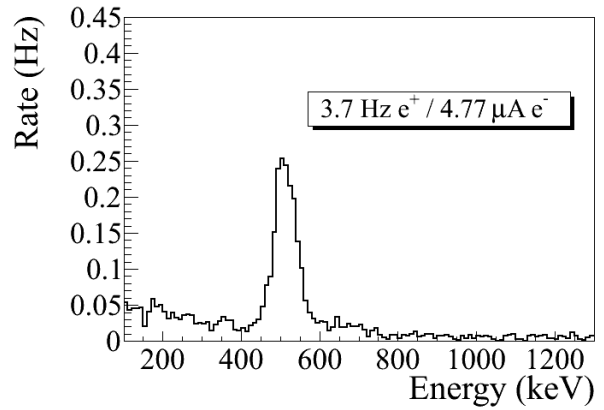
The background subtracted and normalized photon energy spectra observed using two NaI detectors for  $3.00 \pm 0.07$  MeV are shown in Figure 4.8. Figure 4.8 (a) and (b) are the background subtracted spectrum with no coincidence or energy cut. Figure 4.8 (c) and (d) illustrate events observed in coincidence and within a energy window of  $511 \pm 75$  keV for both detectors. The measured positron rate using NaI detectors in coincidence mode was 0.25 Hz for  $3.00 \pm 0.07$  MeV positrons.

## 4.5 The Positron Production Runs

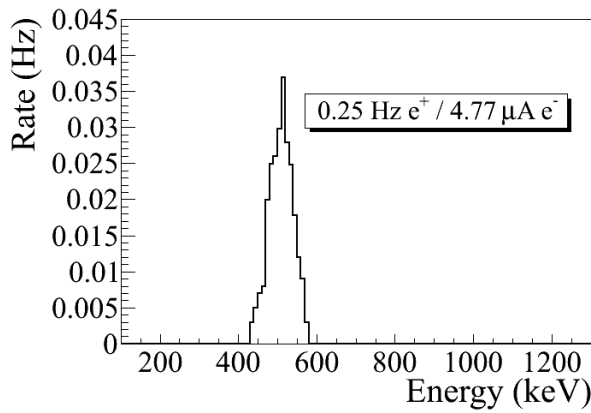
The annihilation target T2 is insertable into the beamline and placed inside a 6-way cross that has horizontal sides vacuum sealed with 1 mil stainless steel windows. Positrons intercepting T2 thermalise, annihilate, and produce 511 keV photon pairs back-to-back.



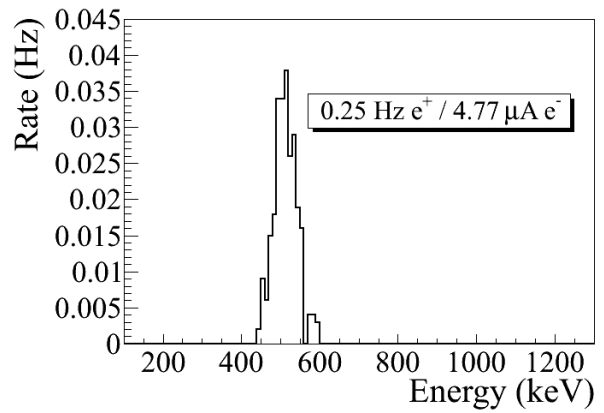
(a)



(b)



(c)



(d)

Figure 4.8: Photon spectrum of NaI detectors after background subtraction created by 3 MeV positrons incident on T2. (a) and (b) are spectrum after background subtractions. (c) and (d) are the spectrum of events coincident in both detectors in 511 keV peaks.

These photons are detected by two NaI detectors facing T2 and shielded with Pb bricks as shown in Figure 4.9. The background was measured by retracting T2 thereby allowing positrons to exit the beamline and be absorbed by the beam dump.

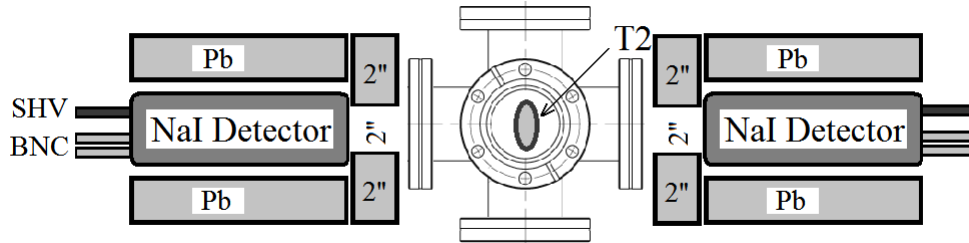
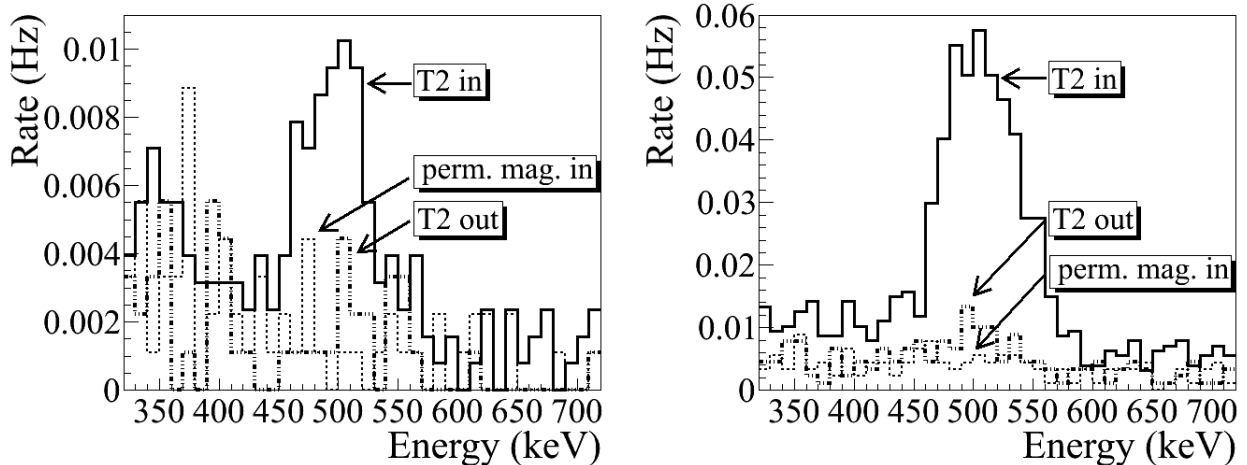


Figure 4.9: Positron detection using T2 and NaI detectors.

As shown in Figure 4.10, a 511 keV peak was observed (solid line) when T2 was in. A permanent dipole magnet was placed on the beamline after Q10 to deflect charged particles on the accelerator side preventing them from entering the shielded cell. The peak was not observed (dashed line) when T2 was in and the permanent magnet was used. The peak was also not observed (dotted dashed line) when T2 and the permanent magnet were removed. Thus, one may argue that the observed peak is due to positrons annihilating in T2.



(a) Original spectrum on left NaI.

(b) Original spectrum on right NaI.

Figure 4.10: Photon spectrum when a permanent dipole magnet is inserted along with T2 (dashed line), dipole out and T2 in (solid line), and dipole removed and T2 out (dotted dashed line). The positron energy incident on the T2 was  $2.15 \pm 0.06$  MeV.

Table 4.4: Positron to Electron Rate Ratio.

Energy	Positron to Electron Ratio	Systematic Error
$1.02 \pm 0.03$	$(0.19 \pm 0.19) \times 10^{-16}$	57.3 %
$2.15 \pm 0.06$	$(0.69 \pm 0.24) \times 10^{-16}$	5.8 %
$3.00 \pm 0.07$	$(8.25 \pm 0.96) \times 10^{-15}$	2.7 %
$4.02 \pm 0.07$	$(4.20 \pm 0.80) \times 10^{-15}$	2.7 %
$5.00 \pm 0.06$	$(0.62 \pm 0.16) \times 10^{-16}$	6.7 %

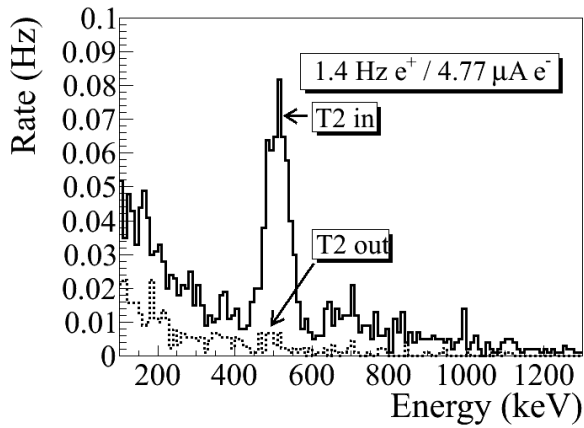
The normalized photon energy spectra observed by two NaI detectors are shown in Figure 4.11 when T2 was both in (signal) and out (background) of the beamline. Figure 4.11 (c) and (d) illustrate the events observed when 511 keV photons were required in both detectors. The signal is indicated by the solid line and background by dashed line.

## 4.6 Positron Rate Estimation in OR Mode

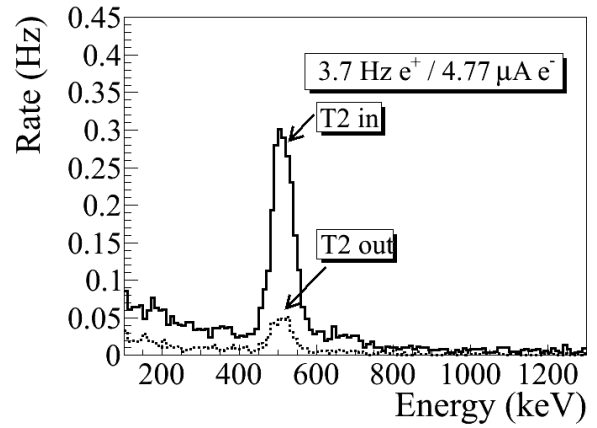
The positron rate was also measured by running NaI detectors in OR mode and the photon spectrum are shown in Figure 4.12 for  $2.15 \pm 0.06$  MeV positrons incident on T2. The rate was 0.21 Hz for left and 0.35 Hz right NaI detectors in OR mode while the rate in coincidence (AND) mode was 0.028 Hz.

## 4.7 Positron to Electron Ratio

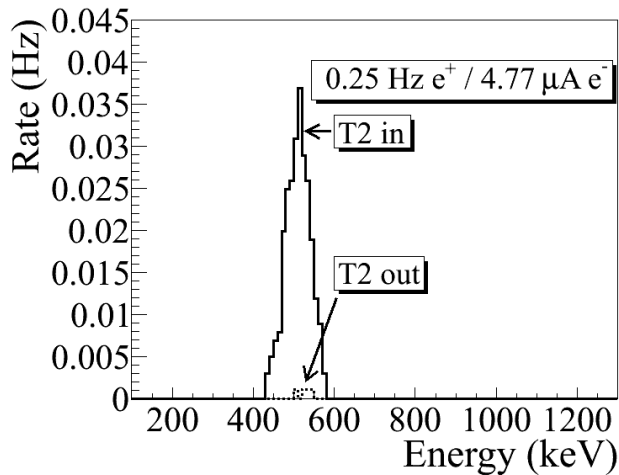
The ratios of positrons detected using NaI detectors in coincidence mode to the electrons impinging on T1 at different energies are given in Table 4.4 and Figure 4.13. A simulation was used to estimate the systematic error of the positrons at different energies. The ratio errors are calculated by propagating the statistical errors of positron and electron rates.



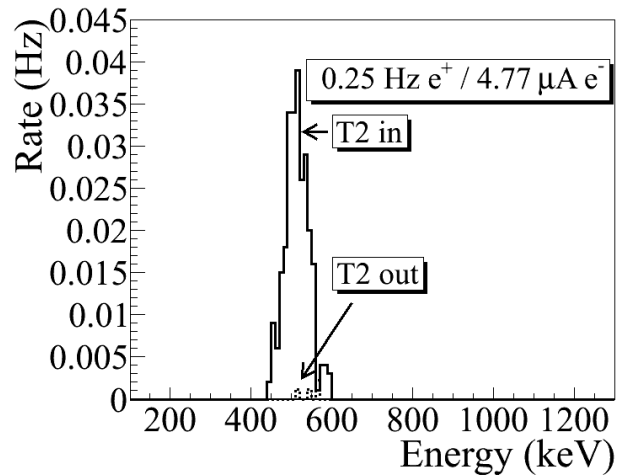
(a) Original spectrum on left NaI.



(b) Original spectrum on right NaI.



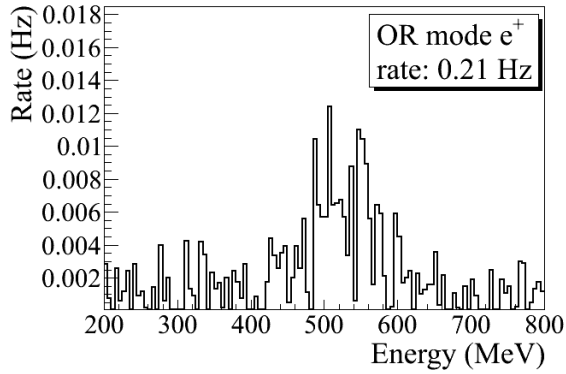
(c) Spectrum with cut on left NaI.



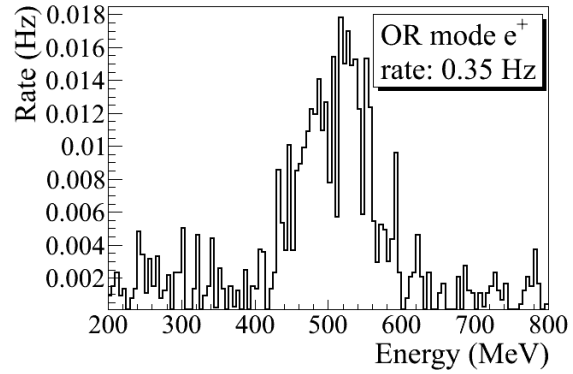
(d) Spectrum with cut on right NaI.

Figure 4.11: The time normalized spectra of photons created by 3 MeV positrons incident on T2. In the top row are original spectrum and in the bottom row are spectrum of incidents happened in the 511 keV peak coincidentally in both detectors. The positron beam energy incident on the T2 was  $3.00 \pm 0.06$  MeV.





(a) Left NaI detector.



(b) Right NaI detector.

Figure 4.12: The positron rates for  $2.15 \pm 0.06$  MeV incident electrons measured by running NaI detectors in OR mode. The rate was 0.21 Hz for left and 0.35 Hz right NaI detectors in OR mode while the rate in coincidence (AND) mode was 0.028 Hz.

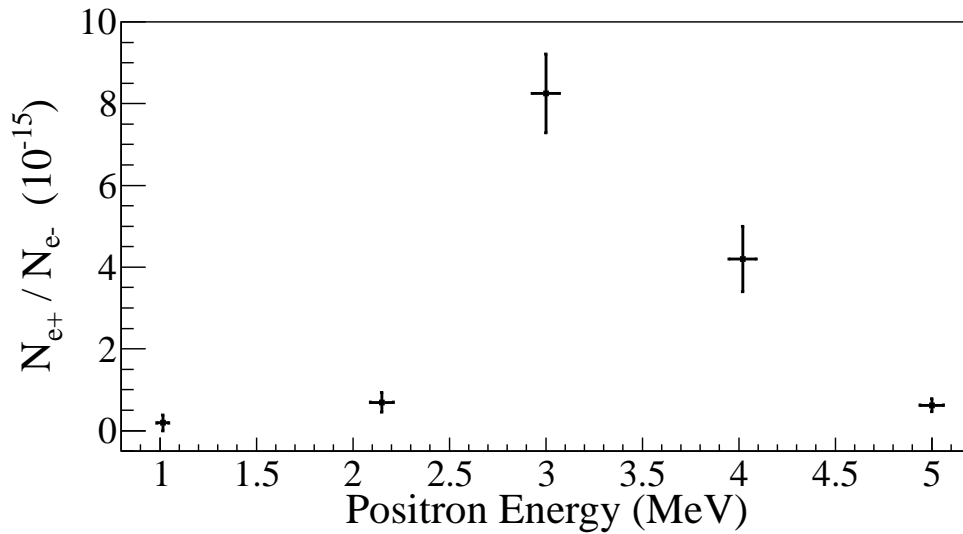


Figure 4.13: The ratios of positrons detected by NaI detectors in coincidence mode to the electrons impinging T1.

# Chapter 5

## Conclusions and Suggestions

A new High Repetition Rate Linac (HRRL) beamline has been successfully reconfigured to produce and transport positrons to the experimental cell. The electron beam energy profile and emittance of the HRRL were measured using a Faraday cup and an OTR based diagnostic system. Positrons generated when the electron beam impinged on a tungsten target (T1) were transported to another tungsten target, T2. The 511 keV photons created inside T2 by the annihilated positrons were detected using two NaI detectors. The positron beam creation, beam loss in the transportation, and detection process were studied using the simulation package G4beamline and compared to this experiment.

An OTR based diagnostic tool was designed, constructed, and used to measure the beam emittance of the HRRL. The electron spatial profile measured using the OTR system was not described by a Gaussian distribution but by a super Gaussian or Lorentzian distribution. The projected emittances of the HRRL were measured to be less than  $0.4 \mu\text{m}$  by the OTR based tool using the quadrupole scanning method when accelerating electrons to an energy of 15 MeV.

The positron detection system was constructed using two NaI detectors and a 1.016 mm thick retractable tungsten target placed in the 6-way cross. Positrons were measured at energies between 1 and 5 MeV as illustrated by the hollow diamond symbols in Figure 5.1. The ratio of positrons detected on NaI detectors to electrons incident on T1 is on the order of  $10^{-15}$ . The ratio is the highest near 3 MeV. The simulation shown in Figure 5.1 predicts the positron production efficiency for the energies measured in this experiment. The simulation includes the measured initial electron energy profile, beam losses during transportation, annihilation in T2, and detection efficiencies. While the simulation result agrees with the

experiment in that the peak energy distribution is near 3 MeV, it predicts a higher positron to electron ratio as shown in Figure 5.1.

The ratio of the positrons contained within the beampipe to the 511 keV photons detected in coincidence mode when the dipoles were set to bend 3 MeV positrons is predicted to be 1655:1 by the simulation. The ratio of the positrons on T2 to the 511 keV photons is 620:1 under the same conditions as above. The 3 MeV positron rate measured in experiment was 0.25 Hz when the HRRL was operated at a 300 Hz repetition rate, 100 mA peak current, and 300 ns (FWHM) RF macro pulse length. Based on this simulation, a measured 0.25 Hz coincidence rate by the NaI detectors would correspond to a 155 Hz positron rate incident on T2. The observed positron to electron ratio was insensitive to the quadrupole triplet collection field setting. Section 3.5 indicates that the solid angle subtended by the quad entrance window approximated the positron loss. Since positrons have a larger angular distribution, perhaps a solenoid may be a better option to improve the collection efficiency. Positioning the target T1 at the entrance of quad or solenoid may be the optimal choice for capturing positrons.

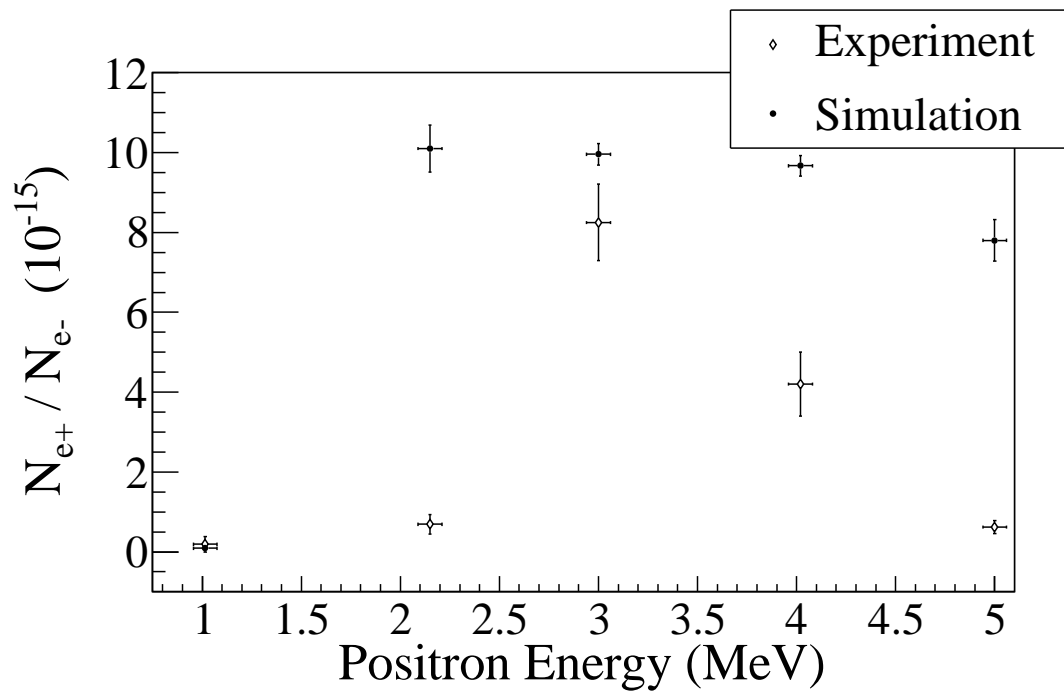


Figure 5.1: Ratio of positrons detected to electrons measured in the experiment (hollow diamond) and simulation (full circle).

# Appendix A

## The Electron Beam Energy Scan

The HRRL electron beam energy was scanned using a dipole magnet by bending the electron beam by  $45^\circ$  to a Faraday cup. The dipole magnet coil current and the electron beam current observed with the Faraday cup is given in the following table.

Table A.1: Dipole Magnet Mapping Data.

<b>Dipole Magnet Coil Current (A)</b>	<b>Faraday Cup Current (mA)</b>	<b>Electron Beam Energy (MeV)</b>
8	0.5	4.3119
9	0.6	4.8896
10	0.67	5.4570
11	0.716	6.0141
12	0.752	6.5610
13	0.828	7.0975
14	0.896	7.6238
15	1.112	8.1399
16	1.328	8.6456
17	1.624	9.1411
18	1.896	9.6262
19	2.448	10.1012
20	3.36	10.5658

*Continued on next page*

Table A.1 – *Continued from previous page*

<b>Dipole Magnet Coil Current (A)</b>	<b>Faraday Cup Current (mA)</b>	<b>Electron Beam Energy (MeV)</b>
21	4.82	11.0201
22	6.58	11.4642
22.2	7.88	11.5518
22.5	9.24	11.6824
22.7	10.0	11.7690
23	10.2	11.8980
23.1	11.2	11.9408
23.2	11.56	11.9836
23.3	13.04	12.0262
23.5	13.2	12.1111
23.8	13.04	12.2377
24	13.48	12.3216
24.2	12.36	12.4050
24.5	11.24	12.5295
24.7	10.2	12.6119
25	10.28	12.7348
25.1	8.6	12.7756
25.2	6.92	12.8162
25.5	6.2	12.9376
25.7	4.84	13.0180
26	3.64	13.1378
26.5	1.82	13.3354
27	1.28	13.5305

*Continued on next page*

Table A.1 – *Continued from previous page*

<b>Dipole Magnet Coil Current (A)</b>	<b>Faraday Cup Current (mA)</b>	<b>Electron Beam Energy (MeV)</b>
28	0.56	13.9129
29	0.364	14.2850
30	0.364	14.6469

# Appendix B

## MATLAB Scripts for Calculating Emittance

The emittance of the HRRL was analyzed using MATLAB. The main script “Emit\_Calc.m” loads and digitize electron beam images. 2D beam is projected to x and y axes and the rms values of the projections are calculated by fitting super Gaussians using a subscript, “Sup-Gau\_devsum.m”. The rms values are sent to another subscript “Emit\_Parabola\_Fit\_kl\_XProjection”. The subscript “Emit\_Parabola\_Fit\_kl\_XProjection” fits parabolic functions, plots the fit and calculate the emittance and Twiss parameters.

### B.1 Emittance Calculator

```
% Emit_Calc.m
% Reads images from files and digitize images.
% Fits a super Gaussian funtion on the projection, get the rms values.
% Then pass them to fit parabola
%
% April-2011
% Sadiq Setiniyaz

clc;
clear
```



```

me = 0.511; % electron rest mass in MeV
%En = 14; %enter beam energy here in MeV unit.
En = 14.9985 ; %14.9985 MeV energy at Mar 17th, 2011.
En_er = En*0.1; % Assume 5% error on Energy
L = 0.08; % pole face is 8 cm long in z direction.
R_Bore = 0.0254; %Radius of the Bore aperture = center to pole face = 1 inch.
%L_ef = L + R_Bore;
%I_max_neg = -10; %enter smallest negative scan current. Here -7 Amps
%I_max_pos = 7; %enter biggest positive scan current. Here 10 Amps
I_start=-3.0; % Scan starting current
%I_end=-2.0; % Scan ending current
I_increment=0.2;
scan_current_number=31; % do 13 scan.
scan_times=7;

%for ii = 1:scan_step
%   I(ii) = I_start + (ii-1)*I_increment;
%end

p = sqrt(En*En - me*me)/1000;% e- momentum in GeV/c

%%%%%%%%%%%%%%%%%%%%%%%%%%%%%%%%%%%%%%%%%%%%%%%%%%%%%%%%%%%%%%%%%%%%%%%%
% Enter the distance from the center of the quad to the screen
S12=3.1;%(in m unit) S12(q4)=1.875 cm. S12(q1)=3.10 cm
erS12 = 0.005; % assume 51 mm error.
%%%%%%%%%%%%%%%%%%%%%%%%%%%%%%%%%%%%%%%%%%%%%%%%%%%%%%%%%%%%%%%%%%%%%%%%

```

```
%%%%%%%%%%%%%%%%%%%%%%%%%%%%%%%%%%%%%%%%%%%%%%%%%%%%%%%%%%%%%%%%%%%%%%%%
```

```
%Enter calibration here:
```

```
calibration_x=0.04327*0.001; %m/px
```

```
calibration_y=0.04204*0.001; %m/px
```

```
er_calibration_x=0.00016*0.001;
```

```
er_calibration_y=0.00018*0.001;
```

```
%%%%%%%%%%%%%%%%%%%%%%%%%%%%%%%%%%%%%%%%%%%%%%%%%%%%%%%%%%%%%%%%%%%%%%%%
```

```
disp('Reading image ...')
```

```
% Get image for background. For background RF is on, gun is off.
```

```
bg1 = imread('Scan_1\RF_on_Gun_off_bg.bmp');
```

```
bg2 = imread('Scan_2\RF_on_Gun_off_bg.bmp');
```

```
bg3 = imread('Scan_3\RF_on_Gun_off_bg.bmp');
```

```
bg4 = imread('Scan_4\RF_on_Gun_off_bg.bmp');
```

```
bg5 = imread('Scan_5\RF_on_Gun_off_bg.bmp');
```

```
bg6 = imread('Scan_6\RF_on_Gun_off_bg.bmp');
```

```
bg7 = imread('Scan_7\RF_on_Gun_off_bg.bmp');
```

```
% Averaging background.
```

```
bg = (bg1+bg2+bg3+bg4+bg5+bg6+bg7+bg7+bg7)/7;
```

```
imd_bg = double(bg(:,:,1));
```

```
for ii=1:scan_times
```

```
switch ii
```

```
case 1
```

```
addpath(genpath('\Scan_1'));
```

```
case 2
```

```
addpath(genpath('\Scan_2'));
```

```

case 3
    addpath(genpath('\Scan_3'));
case 4
    addpath(genpath('\Scan_4'));
case 5
    addpath(genpath('\Scan_5'));
case 6
    addpath(genpath('\Scan_6'));
case 7
    addpath(genpath('\Scan_7'));
end

% Read OTR images.
for scan = 1:scan_current_number;
    thisfilename=ii;
    imNo = ii;
    I(scan) = I_start + (scan-1)*I_increment;
    switch scan
        case 1
            % Devide the effetive length by 100 to convert to meter unit.
            im = imread('negative\11.bmp');
            tifname='11';
            L_ef(scan) = 9.95/100;
            Er_L_ef(scan) = 0.17/100;
        case 2
            im = imread('negative\12.bmp'); % reading 1.png
            tifname='12';
            L_ef(scan) = 9.91/100;
    end
end

```

```
Er_L_ef(scan) = 0.16/100;
case 3
im = imread('negative\13.bmp');
tifname='13';
L_ef(scan) = 9.91/100;
Er_L_ef(scan) = 0.16/100;
case 4
im = imread('negative\14.bmp');
tifname='14';
L_ef(scan) = 9.85/100;
Er_L_ef(scan) = 0.14/100;
case 5
im = imread('negative\15.bmp');
tifname='15';
L_ef(scan) = 9.85/100;
Er_L_ef(scan) = 0.16/100;
case 6
im = imread('negative\16.bmp');
tifname='16';
L_ef(scan) = 9.87/100;
Er_L_ef(scan) = 0.19/100;
case 7
im = imread('negative\17.bmp');
tifname='17';
L_ef(scan) = 9.82/100;
Er_L_ef(scan) = 0.19/100;
case 8
im = imread('negative\18.bmp');
```

```

       .tifname='18';
        L_ef(scan) = 9.86/100;
        Er_L_ef(scan) = 0.17/100;

    end

    sg = im; % reading 1.png
    imd_sg = double(sg(:,:,1));
    pic = (imd_sg-imd_bg);
    %imd = imd_sg;
    %imd = imd_bg;

% Noise Cleaning.
% Getting rid of the dead pixels.
% If there is sudden increase in the pixel brightness,
% Then use the pixel brightness of the earlier pixel.
for i = 3:768
for j = 3:576
    if pic(j,i)>500
        pic(j,i)=pic(j-1,i);
    elseif pic(j,i)-pic(j-2,i)>20
        pic(j,i)=pic(j-1,i);
    end
end
end

% Determine image size in pixels.
dim=size(pic);
%dim=size(imd);
dim_x = dim(1);

```

```

dim_y = dim(2);

xunit='m';
yunit='m';

% Beam transverse profiles.
profx = sum(pic,1); % make x projection
profy = sum(pic,2)'; % make y projection

xbins=size(profx);
ybins=size(profy);
x=(1:1:xbins(2));
y=(1:1:ybins(2));

% Set Gaussian fit range.
xl = 1;
xr = 766;
yl = 1;
yr = 576;

% Checking.
%plot(x,profx,'k');
%hold on;
%plot(y,profy,'k');
%hold on;

% Initialize fit parameters.
% a1= base. a2 = A; amplitude. a3 = mean. a4 = D; sigma_0. a5 = N;

```

```

a1 = 100;
a2 = 7700;
a3 = 280;
a4 = 39;
a5 = 1;

% SupGau = a(1)+a(2)*exp(-abs(X-a(3))/(a(4))).^a(5); % super gaussian.
% Putting the parameters together.
a0 = [a1,a2,a3,a4,a5];
% Setting fit criteria and use fminsearch optimization.
opts = optimset('TolX',1e-4,'MaxFunEvals',10000,'MaxIter',10000,'Display','on');
% Pass fit parameters to SupGau_devsum.
[fitpara_x,fval_x,flag_x,err_x] = fminsearch(@SupGau_devsum,a0,opts,x,prof_x);
[fitpara_y,fval_y,flag_y,err_y] = fminsearch(@SupGau_devsum,a0,opts,y,prof_y);
% Get the fit parameters of x profile.
base_x = fitpara_x(1);
amplitude_x = fitpara_x(2);
peak_center_x = fitpara_x(3);
sig0_x = fitpara_x(4);
N_x = fitpara_x(5);
sig_x(scan,imNo) = sig0_x*(pi/2).^(2/fitpara_x(5)-1);
% Get the fit parameters of y profile
base_y = fitpara_y(1);
amplitude_y = fitpara_y(2);
peak_center_y = fitpara_y(3);
sig0_y = fitpara_y(4);
N_y = fitpara_y(5);
sig_y(scan,imNo) = sig0_y*(pi/2).^(2/fitpara_y(5)-1);

```

```

% Printing out parameters to check.
string_x = [
    num2str(I(scan),' %2.2f'),' ', ...
    num2str(imNo,'%d'),' ', ...
    num2str(base_x,'%12.2f'),' ', ...
    num2str(amplitude_x,'%12.f'),' ', ...
    num2str(peak_center_x,'%12.2f'),' ', ...
    num2str(N_x,'%12.4f'),' ', ...
    num2str(sig0_x,'%12.2f'),' ', ...
    num2str(sig_x(scan,imNo),'%12.2f'),' ', ...
];
%disp(string_x);
string_y = [
    num2str(I(scan),' %2.2f'),' ', ...
    num2str(imNo,'%d'),' ', ...
    num2str(base_y,'%12.2f'),' ', ...
    num2str(amplitude_y,'%12.f'),' ', ...
    num2str(peak_center_y,'%12.2f'),' ', ...
    num2str(N_y,'%12.4f'),' ', ...
    num2str(sig0_y,'%12.2f'),' ', ...
    num2str(sig_y(scan,imNo),'%12.2f'),' ', ...
];
%disp(string_y);
%sig

% Plot to check.
%plot(x,prof_x,'k');

```



```

%hold on;
%plot(y,profy,'k');
%hold on;

% Construct fit curve from the fit parameters.
y_fit_x = fitpara_x(1)+fitpara_x(2)*exp( -0.5*(abs(x-fitpara_x(3))/
(fitpara_x(4))).^fitpara_x(5) );
y_fit_y = fitpara_y(1)+fitpara_y(2)*exp( -0.5*(abs(y-fitpara_y(3))/
(fitpara_y(4))).^fitpara_y(5) );

%plot(x,y_fit_x,'r');

%plot(y,y_fit_y,'r');
drawnow
end
end

for scan=1:scan_current_number

% Find mean and standar deviation.
sig_mean_x(scan) = mean(sig_x(scan,:));
sig_mean_y(scan) = mean(sig_y(scan,:));
sig_x_er(scan)   = std(sig_x(scan,:));
sig_y_er(scan)   = std(sig_y(scan,:));

% Converting from pixels to length (in m unit).
sig_mean_x(scan)=sig_mean_x(scan)*calibration_x; %

```

```

sig_mean_y(scan)=sig_mean_y(scan)*calibration_y; %
sig_x_er(scan)= sqrt((sig_x_er(scan)*calibration_x).^2+(sig_mean_x(scan)*
er_calibration_x).^2);
sig_y_er(scan)= sqrt((sig_y_er(scan)*calibration_y).^2+(sig_mean_y(scan)*
er_calibration_y).^2);

% Squared sigma.
sig_sqr_x(scan) = sig_mean_x(scan)*sig_mean_x(scan);
sig_sqr_x_er(scan) = 2*sig_mean_x(scan)*sig_x_er(scan);
sig_sqr_y(scan) = sig_mean_y(scan)*sig_mean_y(scan);
sig_sqr_y_er(scan) = 2*sig_mean_y(scan)*sig_y_er(scan);

%I(scan) = I_start + (scan-1)*I_increment;
%plot(I,sig_mean,'r');
%Get the quarupole strength and its error from the dipole current.
k1(scan) =0.2998*(3.6*0.0001+1945*0.000001*I(scan))/(0.0254*p);

k1_Er(1) =0.2998*((3.6+1.3)*0.0001+(1945+2)*0.000001*I(scan))/(0.0254*p);
k1_Er(2) =0.2998*((3.6-1.3)*0.0001+(1945+2)*0.000001*I(scan))/(0.0254*p);
k1_Er(3) =0.2998*((3.6+1.3)*0.0001+(1945-2)*0.000001*I(scan))/(0.0254*p);
k1_Er(4) =0.2998*((3.6-1.3)*0.0001+(1945-2)*0.000001*I(scan))/(0.0254*p);
er_k1(1)=abs(k1(scan)-k1_Er(1));
er_k1(2)=abs(k1(scan)-k1_Er(2));
er_k1(3)=abs(k1(scan)-k1_Er(3));
er_k1(4)=abs(k1(scan)-k1_Er(4));

k1_er(scan)=max(er_k1);

```

```

k1L(scan) = L_ef(scan)*k1(scan); %k1*L
er_k1L(scan) = sqrt((L_ef(scan)*k1_er(scan) )^2+(Er_L_ef(scan)*k1(scan))^2);
%er_k1L(scan) = L_ef*k1_er(scan);

% Put the parameters together to pass to parabolic fits
FitDatX = [k1L',er_k1L',sig_sqr_x',sig_sqr_x_er'];
FitDatY = [k1L',er_k1L',sig_sqr_y',sig_sqr_y_er'];

end

X_fit_data = fopen('X_fit_data.txt','w');
Y_fit_data = fopen('Y_fit_data.txt','w');
fprintf(X_fit_data,'%4f %4f %4f %4f \n',k1L(16:31)',er_k1L(16:31)',
sig_sqr_x(16:31)*10^6',sig_sqr_x_er(16:31)*10^6');
fprintf(Y_fit_data,'%4f %4f %4f %4f \n',k1L(2:15)',er_k1L(2:15)',
sig_sqr_y(2:15)*10^6', sig_sqr_y_er(2:15)*10^6');
fprintf(X_fit_data,'%4f %4f %4f \n',k1L(16:31)', sig_sqr_x(16:31) '*10^6,
sig_sqr_x_er(16:31) '*10^6);
fprintf(Y_fit_data,'%4f %4f %4f \n',k1L(2:15)', sig_sqr_y(2:15) '*10^6,
sig_sqr_y_er(2:15) '*10^6);
fclose(X_fit_data);
fclose(Y_fit_data);

% Converting to cgs (mm and mrad) units.
[k1L(16:31)' sig_sqr_x(16:31) '*10^6 sig_sqr_x_er(16:31) '*10^6]
[k1L(2:15)' sig_sqr_y(2:15) '*10^6 sig_sqr_y_er(2:15) '*10^6]

```

```

%Emit_Parabola_Fit_kl_XProjection(k1L,er_k1L,sig_sqr_x,sig_sqr_x_er,me,En,
S12,erS12,scan_current_number);
%Emit_Parabola_Fit_kl_YProjection(k1L,er_k1L,sig_sqr_y,sig_sqr_y_er,me,En,
S12,erS12,scan_current_number);
Emit_Parabola_Fit_kl_XProjection(k1L(16:31),er_k1L(16:31),
sig_sqr_x(16:31)*10^6,sig_sqr_x_er(16:31)*10^6,me,En,En_er,S12,erS12,16);
Emit_Parabola_Fit_kl_YProjection(k1L(2:15) ,er_k1L(2:15),
sig_sqr_y(2:15)*10^6, sig_sqr_y_er(2:15)*10^6, me,En,En_er,S12,erS12,14);

```

## B.2 Super Gaussian Fit

```

function chisq = SupGau_devsum(a,X,Y)
% a(1) = base
% a(2) = A; %amplitude
% a(3) = x0; %center
% a(4) = D; %sigma_0
% a(5) = N; %N=2 is nomal Guassian.
           %N<super Gaussian (sharp top).
           %N>Flat top shape Gaussian.
SupGau = a(1)+a(2)*exp( -0.5*(abs(X-a(3))/(a(4))).^a(5) ); % super Gaussian
csq = (Y - SupGau).^2;
chisq = sum(csq);
return

```

## B.3 Parabolic Fit

```

function varargout = Emit_Parabola_Fit_kl_XProjection(x,erx,y,ery,me,En,

```

```

En_er,S12,erS12,NumPoints)

%x
%y
%ery

order = 2; % second order fit
ParNum = order + 1;

% finding row matrix beta
for k=1:ParNum
for i=1:NumPoints
    f(k)=power(x(i),k-1);
    %fprintf(' i=%d f(%d)=%g \t',i,k,f(k));
    beta_element(k,i)=y(i)*f(k)/(ery(i)*ery(i));
    %fprintf('y(i=%d)=%g ery(i=%d)=%g \n',i,y(i),i,ery(i));
    %fprintf('beta(k=%d,i=%d)=%g \n',k,i,beta_element(k,i));
    beta(k)=sum(beta_element(k,:));
    %fprintf('beta_element(%d,%d)=%g
    %beta(%d)=%g\n',k,i,beta_element(k,i),k,beta(k));
end
end
%beta

% finding matrix alpha
for k=1:ParNum
for l=1:ParNum
    for i=1:NumPoints

```

```

    f(k)=power(x(i),k-1);
    f(l)=power(x(i),l-1);
    alpha_element(k,l,i)=f(k)*f(l)/(ery(i)*ery(i));
    alpha(k,l)=sum(alpha_element(k,l,:));
    %fprintf('alpha_element(%d,%d,%d)=%g alpha(%d,%d)=%g\n',k,l,i,
    alpha_element(k,l,i),k,l,alpha(k,l));
end
end
end
%alpha

%To find fit parameters, need to invert matrix alpha.
alpha_invert = inv(alpha);
%alpha_invert

% The fit is  $y = a(1) + a(2)*x + a(3)*x*x$ 
%fit parameters by matrix inversion method
parameter = beta*alpha_invert; %a(1)=parameter(1)
%parameters
fit_m_inver = parameter(1) + parameter(2)*x + parameter(3)*x.*x;
% error on the parameters
er_a = sqrt(diag(alpha_invert));

%fit parameters by MatLab
par = polyfit(x,y,2);
%par
fit_MatLab = par(3) + par(2)*x + par(1)*x.*x;

```

```

%Get Emittance and Twiss parameters from fit
gamma = En/me;
er_gamma = En_er/me;
beta = sqrt(1-1/gamma^2);
er_beta = er_gamma/(gamma^3*beta);

A=parameter(3);
B=-parameter(2)/(2*A);
C=parameter(1)-A*B^2;
erA = er_a(3);
erB = sqrt( (-er_a(2)/(2*A))^2 + (parameter(2)*erA/(2*A^2))^2 );
erC = sqrt((er_a(1))^2 + (-B^2*erA)^2 + (-2*A*B*erB)^2);
fprintf('A=%g+-%g B=%g+-%g C=%g+-%g\n',A,erA,B,erB,C,erC);

emit = sqrt(A*C)/((S12)^2);
er_emit = sqrt( (1/2*A^(-1/2)*A^(1/2)*erA/(S12)^2)^2 +
(1/2*A^(1/2)*A^(-1/2)*erC/(S12)^2)^2 + ( 2*sqrt(A*C)*erS12/(S12)^3)^2 );
emit_n = emit*gamma;
er_emit_n = sqrt((emit*er_gamma*beta)^2+(emit*gamma*er_beta)^2+
(er_emit*gamma*beta)^2);
beta_func = sqrt(A/C);
er_beta_func = sqrt( (1/2*sqrt(1/(A*C))*erA)^2 + (-1/2*sqrt(A/C^3)*erC)^2 );
alpha_func = beta_func*(B + 1/S12);%alpha_func = sqrt(A/C)*(B + 1/S12)
er_alpha_func = sqrt(((B+1/S12)*er_beta_func)^2 + (beta_func*erB)^2 +
(-beta_func*erS12/(S12)^2)^2 );

figure(1)

```

```

set(axes,'FontSize',40)
pardat = errorbar(x,y,ery,'MarkerSize',30,'Marker','.', 'LineStyle','none',...
'LineWidth',3,...
'DisplayName','Data Points',...
'Color',[0 0 1]);
hold on

%Plot fit done by matrix inversion method.
parfit_m_inver = plot(x,fit_m_inver,'r');
set(parfit_m_inver,'LineWidth',3);

legend('Data','Fit');
set(legend,'Position',[0.73 0.75 0.1 0.1]);
set(legend,'FontSize',40);
set(legend,'FontName','Times New Roman');

hx = xlabel('k_{1}L (m^{-1})','FontSize',48,'FontName','Times New Roman');
hy = ylabel('\sigma^2_x (mm^2)','FontSize',48,'FontName','Times New Roman');
box off; % remove the top and right axes

%set(gca,'ticklength',4*get(gca,'ticklength'));
set(gca,'ticklength',[0.06 0.9]);
fit=title('');
%fit=title('15.6 MeV, X-Projection: k_{1}L vs \sigma^2');
set(fit,'FontSize',24,'FontWeight','bold','FontName','Times New Roman');
axis([-0.05 0.55 2.3 3.2]); %axis([xmin xmax ymin ymax])
%axis('FontSize',28);

```



```

saveas(fit,'Emit_Calc_plots\par_fit_x.fig','fig');
saveas(fit,'Emit_Calc_plots\par_fit_x.eps','epsc');
saveas(fit,'C:\Users\sadiq\Desktop\IPAC12\Paper\par_fit_x.eps','epsc');
saveas(fit,'Emit_Calc_plots\par_fit_x.png','png');
drawnow

fprintf('x-projection:\n\nemit=%.3f +- %.3f mm*mrad, emit_norm=%.2f +-
%.2f mm*mrad \n\n', emit, er_emit, emit_n, er_emit_n);
fprintf('beta=%.2f +- %.2f m, alpha=%.2f +- %.2f rad \n\n', beta_func,
er_beta_func, alpha_func, er_alpha_func);
fprintf('parabola fit for y-projection (y in mm unit): \n y = (%.5f +-.5f)
+ (%.5f+-.5f)*x + (%.5f+-.5f)*x.*x \n\n', parameter(1),er_a(1),
parameter(2),er_a(2), parameter(3),er_a(3));
return

```

# References

- [1] S. Chemerisov. and C.D. Jonah, “Generation of High Intensity Thermal Positron Beams Using A 20-MeV Electron Linac”, in *AIP Conference Proceedings*, **1160**, Newport News, Virginia, 2009, pp. 87-93.
- [2] I. Procházka, “Positron Annihilation Spectroscopy”, in *Materials Structure*, **8**, number 2 (2001), pp. 55-60.
- [3] M.N. Rosenbluth, “High Energy Elastic Scattering of Electrons on Protons”, *Phys. Rev.*, **79**, 615 (1950).
- [4] R.C. Walker, B.W. Filippone, J. Jourdan, R. Milner, R. McKeown, D. Potterveld, L. Andivahis, R. Arnold, D. Benton. P. Bosted, G. deChambrier, A. Lung, S.E. Rock, Z.M. Szalata, A. Para, F. Dietrich, K. Van Bibber, J. Button-Shafer, B. Debebe, R.S Hicks., S. Dasu, P. de Barbaro, A. Bodek, H. Harada, M.W. Krasny, K. Lang, E.M. Riordan, R. Gearhart, L.W. Whitlow, and J. Alster, “Measurements of The Proton Elastic Form Factors for  $1 \leq Q^2 \leq 3$  (GeV/c)<sup>2</sup> at SLAC”, *Phys. Rev. D*, **49**, 5671-5689 (1994).
- [5] J. Arrington, “How Well Do We Know The Electromagnetic Form Factors of The Proton?”, *Phys. Rev. C*, **68**, 034325-034338 (2003).
- [6] R.C. Walker, *Ph.D. Thesis*, California Institute of Technology (1989).
- [7] J. Arrington, V.F. Dmitriev, R.J. Holt, D.M. Nikolenko, I.A. Rachek, Yu.V. Shestakov, V.N. Stibunov, D.K. Toporkov, and H. de Vries, “Two-photon Exchange and Elastic Scattering of Electrons/Positrons on The Proton”, *Proposal for an experiment at VEPP-3*, 2004.
- [8] H.W. Koch and J.W Motz, “Bremsstrahlung Cross-Section Formulas and Related Data”, *Rev. Mod. Phys.*, **31**, 920-955 (1959).

- [9] K.S. Krane, *Introductory Nuclear Physics.*, John Wiley & Sons, New York, 1988.
- [10] NIST, <http://physics.nist.gov/cgi-bin/Xcom/xcom2>, NIST XCOM, 2013-05-03.
- [11] M. Conte, and W.W. Mackay, *An Introduction to The Physics of Particle Accelerators*, World Scientific, New York, 2008.
- [12] V.L Ginzburg and I.M. Frank, “On The Transition Radiation Theory”, *Sov. Phys. JETP*, **16**, 15 (1964).
- [13] K.T. McDonald and D.P. Russell, “Methods of Emittance Measurement”, *Fron. of Par. Beams Obser. Diag. and Cor.*, **08544**, 1 (1988).
- [14] Y. Kim, A. Andersson, M. Dach, R. Ganter, C. Gough C. Hauri, R. Ischebeck, F. Le Pimpec, M. Paraliiev, M. Pedrozzi T. Schietinger, V. Schlott, B. Steffen, and A.F. Wrulich, “Low Thermal Emittance Measurements at the Low Emittance Gun (LEG) Test Facility”, in *Proc. FEL2008*, **1160**, Gyeongju, Korea, 2008, pp. 110-113.
- [15] D.F.G. Benedetti, B. Buonomo, and D. Filippetto, “Emittance Measurement of The DAFNE Linac Electron Beam”, *Tech. Rep., DAFNE Tech. Not.*, Frascati, Italy (2005).
- [16] S.Y. Lee, *Accelerator Physics*, 2nd ed., World Scientific, Singapore, 2004.
- [17] B. Gitter, “Optical Transition Radiation”, *Tech. Rep.*, Los Angeles, USA, 1992.
- [18] Muons, Inc., <http://public.muonsinc.com/>, 2013-08-08.
- [19] CERN, <http://geant4.cern.ch/>, 2013-08-08.
- [20] Saint-Gobian, <http://www.detectors.saint-gobain.com>, Saint-Gobian Crystals Technical Information Notes, 2013-06-11.
- [21] The MathWorks, Inc., <http://www.mathworks.com/>, 2013-10-31.
- [22] F.J. Decker, “Beam Distribution Beyond RMS”, in *6th Workshop on Beam Instrumentation*, Vancouver, Canada, (1994). pp. 1-7.